Spring 2020

Compaction and Residual Stress Modeling in Composite Manufactured with Automated Fiber Placement

Von Clyde Jamora
Old Dominion University, vjamo001@odu.edu

Recommended Citation

Jamora, Von C.. "Compaction and Residual Stress Modeling in Composite Manufactured with Automated Fiber Placement" (2020). Master of Science (MS), Thesis, Mechanical & Aerospace Engineering, Old Dominion University, DOI: 10.25777/j2pk-ke03
https://digitalcommons.odu.edu/mae_etds/313

COMPACTION AND RESIDUAL STRESS MODELING IN COMPOSITE MANUFACTURED WITH AUTOMATED FIBER PLACEMENT

by

Von Clyde Jamora
B.S May 2018, Old Dominion University

A Thesis Submitted to the Faculty of
Old Dominion University in Partial Fulfillment of the
Requirements for the Degree of

MASTER OF SCIENCE

MECHANICAL AND AEROSPACE ENGINEERING

OLD DOMINION UNIVERSITY
May 2020

Approved by:

Oleksandr Kravchenko (Director)

Krishnanand N. Kaipa (Member)

Mileta M. Tomovic (Member)

Gene Hou (Member)

ABSTRACT

COMPACTION AND RESIDUAL STRESS MODELING IN COMPOSITE MANUFACTURED WITH AUTOMATED FIBER PLACEMENT

Von Clyde Jamora
Old Dominion University, 2020
Director: Dr. Oleksandr Kravchenko

Automated fiber placement is a state-of-the-art manufacturing process that allows for complex layup patterns and can quickly place, cut, and restart composite tows. However, with this type of manufacturing process layup defects are inevitable, and manufacturing defects propagate after curing. Process modeling is the considered approach for exploring the defect prediction. Two different but related works were conducted, which are the thermochemical and hyperelastic model and the residual deformation model. For the model before cooling, a hyperelastic model and a thermo-chemical were made to simulate the compaction and heat transfer. Temperature dependent properties that are a function of degree of cure and glass transition temperature were made. An exothermic reaction was simulated with the thermo-chemical model which shows the composite temperature exceeds the applied temperature. Currently, the hyperelastic model shows some behavior in manufacturing induced defect deformation. The residual stress analysis involves two tow-steered composite shells, one with overlapping plies and one without. The coefficient of thermal expansion was measured using digital image correlation and homogenized temperature dependent properties was derived from the results. The stacking sequence, orientation, and thickness was used to create a piecewise stiffness matrix on a simple shell element and varying modeling conditions were applied for a more robust model. The results of the residual deformation show that non-linearity and temperature dependence did not affect the resultant geometry. Out-of-roundness data shows that the shells with overlaps can be simulated through shell element while shells without overlaps did not show good qualitative results.

AKNOWLEDGEMENTS

Thank you to all my advisors, my teachers, and my colleagues for teaching me and supporting me. And a special thanks to my friends and family for encouraging me to continue my education.

And special thanks for all the medical staff who has done so much in this time of crisis when the thesis was being made.

TABLE OF CONTENTS

LIST OF FIGURES

CHAPTER 1

INTRODUCTION

Fiber reinforced composites in the study are thermosetting resins with load bearing fibers that exhibit high specific strength and stiffness. Innovations in automated manufacturing of composites have progressed to allow the fabrication of complex layups with variable plies which results in a rapid increase in throughput for advanced composites. Automated fiber placement (AFP) is a state-of-the-art method that allows for the fabrication of advanced composite structures with variable fiber orientations and variable thickness [1]. The process involves automatic deposition and compaction of a tow in a single step [2]. A major source of AFP's versatility comes from the ability to quickly lay, stop, cut, and restart individual fiber bundles [3] which allows for the fiber orientation to vary continuously within a single ply [4]. Unlike other conventional composite manufacturing methods, AFP allows for complex structure manufacturing in curved surfaces [5]. Structures made using AFP offer the tailoring for specific loading conditions while reducing the weight in comparison to conventional layup manufacturing [6]. The capability to fabricate composites using AFP has been available since the 1980s [1] and widely used in the aerospace industry [6], [7]. The increase in demand for composites needs automation as an integral step to a reliable, fast, and efficient manufacturing process for complex structures [8]–[10]. To fully leverages the advantages of the AFP, a greater understanding of the manufacturing process is essential to aid in design and certification of novel prototypes [5].

While there are numerous benefits to AFP, the manual manufacturing of composite is still more prominent [8]. Uncertainties in manufacturing hinder the process and must be analyzed to enhance reproducibility of AFP made composite structures. Defects in the composites are inevitable in the automated fiber manufacturing process [3], [4], [11]. Initial layup defects magnifies into ply deformation and shifts after consolidation [4], [5]. The presence of layup defects, such as gaps and overlaps (Fig. 1), have proven to cause an overall reduction in strength in composites due to the resulting morphology [12], [13] but more research is needed to understand the effects of manufacturing defects on laminate mechanical properties [14]. It is important for the certification of AFP to observe and categorize the defects that are produced during manufacturing [15]. Research into their formation and their effect on material properties is crucial for AFP certification. Microscopy is a practical tool for observing the surface of a composite while computer tomography can identify defects within the structure to better visualize the imperfections caused after manufacturing. With the proper tools, manufacturing defects can be identified and studied to take the steps to minimizing its effects on composite structures. The study will provide a good basis for determining the microscopic descriptors of the damage in terms of variable volume fraction, ply thickness and fiber misalignment. It is important to analyze these defects for their possible causes and how it influences the final product.

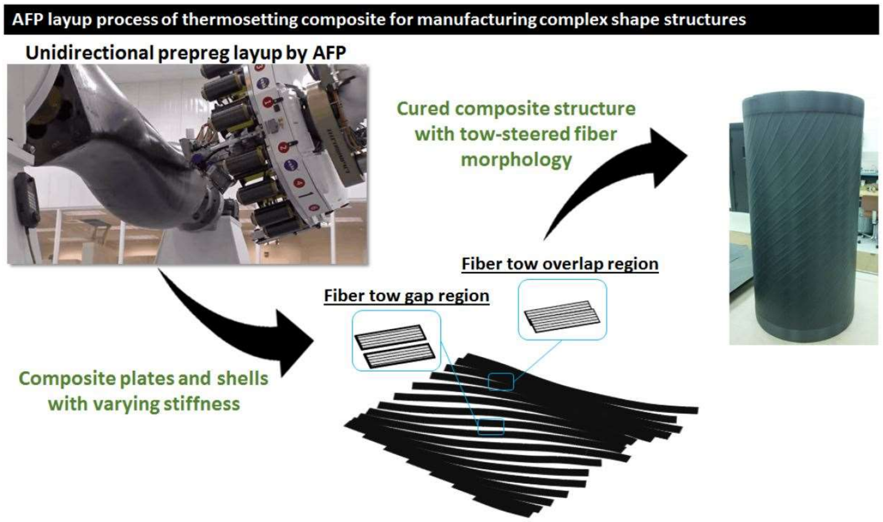

Figure 1. Initial layup defects affecting the morphology of automated fiber placement composites

To fully study the manufacturing phenomenon of AFP made composites, all interconnected physics involved needs to be coupled in a singular model. This include the resin flow, compaction, and the heat transfer throughout the material. The proposed approach for this research is the process modeling through finite element analysis (FEA) using a combination of a thermo-chemical model with a compaction model using visco-hyperelastic constitutive equations. The thermo-chemical model will use a balanced Fourier's heat conduction equation to simulate the heat transfer throughout the composite model. The visco-hyperelastic models consists of two parts, a hyperelastic component and a viscous component. Only a prototype that contains the hyperelastic component will be the focused in this study. Understanding the morphology is an essential step in predicting the damage onset and propagation during the life-time of the composite and its strength [12]. A validated computational model will aid in the design process and reduce the number of trial and error in physical testing. Furthermore, it will provide a platform for determining key parameters for AFP manufacturing. Through these methods, the feasibility of predicting the morphology will be determined and how manufacturing parameters can be optimized for less imperfections. By conducting this research, the goal is to provide a better understanding in AFP made composites.

After onset of gelation during the manufacturing cure cycle, the mechanical properties of composites develop and lead to residual stress formation [16], [17] with a major part of the deformation attributed to the cooling process [18]. Residual stresses accumulate with increasing thickness of the composite and unsymmetrical distribution can cause distortions [19]. It is essential to analyze the residual deformation and the associated thermodynamics for a proper analysis of the manufacturing process of AFP composites. Computational modeling has been shown as an effective tool for supporting the understanding of experimental characterization and manufacturing phenomena in composites [20]–[22]. One of the goals of this research is to establish whether consideration of the cooling process during AFP manufacturing of tow steered shells provide good correlation with experimentally measured residual deformations for geometric imperfections. Specifically, if the complex fiber orientation in AFP composite can be modeled using simple shell elements. The finite element model features numerous elements with varying thickness, stacking sequence and fiber orientations which forms a piecewise stiffness matrix to simulate the complex layup patterns found in the tow-steered composite shell. The effects of temperature dependent lamina properties on a residual deformation analysis of a cylindrical structure with the complex pattern made from AFP has not been studied in depth. Therefore, nonlinearity and the effect of material softening at elevated temperatures were employed to understand their effect in FEA modeling. Finally, the numerical results are compared to experimental out-of-roundness data to validate the approach.

1.1 Literature Review and Background: Tow-Steered Composite Structures

Research has been done to utilize the capabilities of AFP with the recent development of technology such as the Integrated Structural Assembly of Advanced Composites (ISAAC) at NASA Langley [23]. The system involves a large rotating head that can be detached and quickly refitted, which results in adaptability to new task. Previous work by Wu [5] into AFP involves the design and manufacturing of advanced composite prototype shells with complex tow steered patterns. Two cylindrical shells have a nominal 8-ply $[\pm 45, \pm\theta]_S$ layup where θ refers to a ply with varying angles that was steered by ISAAC (Figure 2. ~~Figure 2.~~ One shell was made with all 24 tows placed during each pass of the AFP machine, which was designated as Shell A. The second shell was made using the cut/restart capability of the AFP machine to place individual tows resulting in a more uniform thickness throughout the model. Although both shells have a similar orientation pattern, Shell A contains complex stacking due to overlapping plies, which results in a variable number of plies: from 8 on the sides to reaching maximum of 18 plies on the crown and keel. It should be mentioned that laid up fiber tow overlaps, in the case of Shell A, undergo compaction and consolidation during manufacturing. Therefore, it can be assumed that the actual fiber orientations in the local regions of the overlap do not match the nominal stacking sequences created during deposition [24]. The present shell analysis does not consider changes in fiber orientation due to distortion during compaction and consolidation and implements fiber orientation produced during deposition for the residual deformation analysis. Furthermore, the predicted residual deformations for Shells A and B were found to be different depending on the steered pattern utilized during AFP manufacturing. The design resulted in a structure comparable to an I-beam with the crown and keel akin to the flanges of a beam and the shell sides providing higher shear stiffness to transfer shear loading [6].

The shapes of manufactured AFP shells were measured using a coordinate measurement machine (CMM). A Brown and Sharpe Global Image CMM was used along with PC-DMIS version 3.7 automation software. The CMM probe was a SP600M, with a resolution of 4x10^{-6} in. and a 50 mm and 20 mm by 4 mm spherical ruby tip. The scans were done every 0.75° circumferentially (or approximately 0.106 in.), and every 0.1 in. axially. The measurements are used a metric to measure the computational modeling of the study. The nominal FEM radius that was mentioned are 8.164 in. for Shell A and 8.166 for Shell B which corresponds to the midplane radius [5].

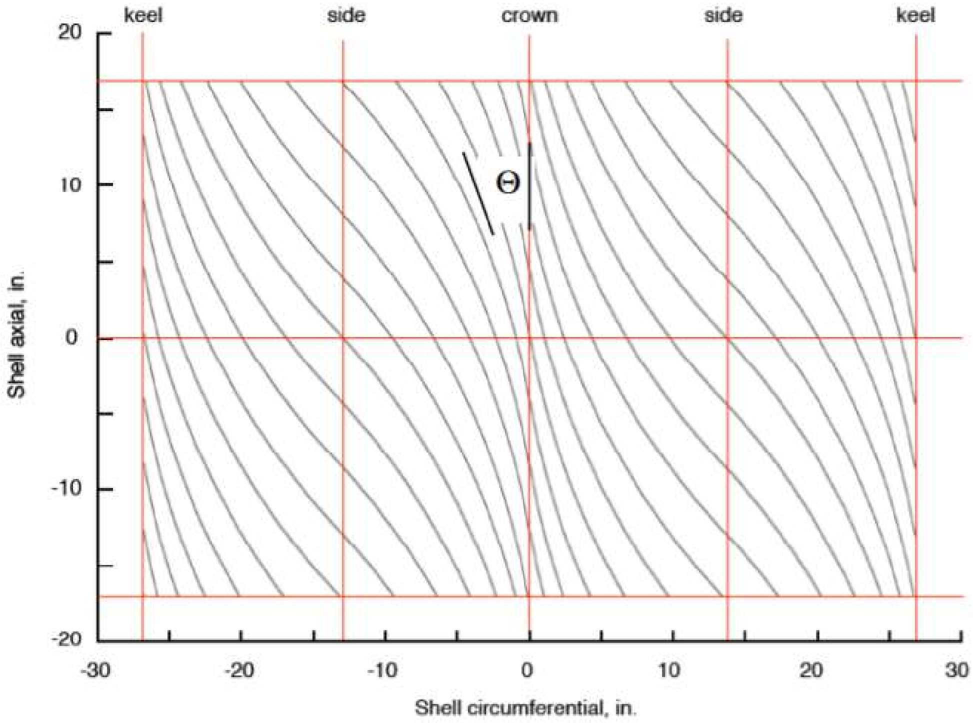

Figure 2. Path of the tow steered plies demonstrating the change of angle from crown to keel [5]

1.2 Thermo-Chemical Process Modeling

For the various interconnected physics that process modeling uses, a significant component is the heat transfer throughout the composite [25]. The thermo-chemical model calculates crucial information such as temperature, resin flow, and the degree of cure. The governing equation of this model comes from a three-dimensional energy balance of Fourier's heat conduction equation Eq. 1.

$$\rho_c c_c \frac{\delta T}{\delta t} + \rho_m c_m V_D \nabla T = \nabla \cdot (k \nabla T) + \rho_m v_m Q_t \frac{d\alpha}{dt} \tag{1}$$

where the subscripts c and m indicate the homogenized composite and the matrix, respectively. The ρ, k, Q_t, v_m, and C indicate the density, thermal conductivity, heat of reaction, fiber volume fraction and the specific heat. Finally, the T, V_D and α are the temperature, Darcy velocity, and the degree of cure, respectively.

While there are numerous methods to simulating the evolution of the cure for a material, the resin kinetics was derived from a modified Arrhenius type equation [26] as shown

$$\frac{d\alpha}{dt} = \begin{cases} (k_1 + k_2\alpha)(1-\alpha)(0.47-\alpha), & \alpha \geq 0.3 \\ k_3(1-\alpha), & \alpha > 0.3 \end{cases} \tag{2}$$

$$k_i = A_i\left(-\frac{\Delta E_i}{RT}\right), i = 1,2,3 \tag{3}$$

where the variables A_i are pre-exponential factors, and ΔE_i are the activation energies. R and T are the gas constants and the absolute temperature.

1.3 Compaction Modeling using Hyperelastic Constitutive Behavior

The process modeling of composites requires a vast amount of interconnected physics to fully simulate the manufacturing of composite structures. A novel approach to modeling the consolidation of uncured composite is using visco-hyperelastic constitutive equations in a finite element software. In the work of Belnoue et al. [27], the compaction modelling component consists of two parts: an elastic model and a viscous model. The elastic model was derived from the works of Limbert and Middleton [28] where they modeled soft connective tissue using transversely isotropic visco-hyperelastic constitutive equations. The same principle can be applied to composites, which exhibit transverse isotropy and show viscous properties during curing and compaction.

The elastic model uses the deformation gradient tensor $\boldsymbol{F}$ to calculate the Cauchy-Green deformation tensor, $\boldsymbol{C}$, and create a constitutive equation based on the Helmholtz free energy function, ψ. This function is only a function of $\boldsymbol{X}$, $\boldsymbol{C}$, $\dot{\boldsymbol{C}}$, and $\boldsymbol{N_0}$ which is the position, Cauchy-Green deformation tensor, the deformation rate, and the material orientation respectively. It is also noteworthy that $\boldsymbol{C}$ is a parameter rather than a variable of ψ. The function can now be used to define the Piola-Kirchhoff stress tensor as:

$$S = S^e + S^v = 2\left(\frac{\partial\psi^e}{\partial\boldsymbol{C}} + \frac{\partial\psi^v}{\partial\dot{C}}\right) \tag{4}$$

It is then possible to form an irreducible integrity bases for $\boldsymbol{C}$, $\dot{\boldsymbol{C}}$, $\boldsymbol{N_0}$ [29]. However, the focus of

$$I_1 = 2{:}\,\boldsymbol{C}, I_2 = \frac{1}{2}[I_1^2 - (1{:}\,\boldsymbol{C}^2)], I_3 = \det(\boldsymbol{C}), I_4 = \boldsymbol{N_0}{:}\,\boldsymbol{C}, I_5 = N_0{:}\,\boldsymbol{C}^2 \tag{5}$$

the study will be on the elastic component only which will use the following five invariants:

Deriving the invariants with respect to the Cauchy-Green deformation tensor yields:

$$\frac{\partial I_1}{\partial C} = I,\ \frac{\partial I_2}{\partial C} = I_1 I - \boldsymbol{C},\ \frac{\partial I_3}{\partial C} = I_3\boldsymbol{C}^{-1},\ \frac{\partial I_4}{\partial C} = \boldsymbol{N_0}, \frac{\partial I_5}{\partial C} = \boldsymbol{a} \otimes C \cdot \boldsymbol{a} + \boldsymbol{C} \cdot \boldsymbol{a} \otimes \boldsymbol{a} \tag{6}$$

where $\boldsymbol{a}$ is the fiber orientation vector. Note that $\boldsymbol{a} \otimes \boldsymbol{a} = \boldsymbol{N_0}$. The focus for the study will be on the hyperelastic portion of the constitutive equation. To further simplify the equation, the Piola-Kirchoff stress tensor can be derived as:

$$S^e = 2\frac{\partial \psi^e}{\partial \boldsymbol{C}} = 2\sum_{\alpha=1}^{5}\left(\frac{\partial \psi^e}{\partial I_\alpha}\frac{\partial I_\alpha}{\partial \boldsymbol{C}}\right) \tag{7}$$

Belnoue et al. [27] then chose to express the ψ^e with the Neo-Hookean elastic of a transversely isotropic material potential from Bonet and Burton [30]:

$$\psi^e = \frac{1}{2}\mu_T(I_1 - 3) - \mu_T\, ln(J) + \frac{1}{2}\lambda(J-1)^2 + \left[(\mu_T - \mu_L) + \frac{\alpha}{4}ln(J) + \frac{\beta}{8}(I_4 - 1)\right](I_4 - 1) + \frac{1}{2}(\mu_T - \mu_L)(I_5 - 1)\,) \tag{8}$$

where $J = \sqrt{I_3}$. The parameters, $\mu_T, \mu_L, \propto, \beta$ and λ can be expressed as functions of common engineering constants [28], [31] where the subscript 1 denotes the fiber direction and subscripts 2 and 3 are equal due to transverse isotropy:

$$\lambda = \frac{E_2(\nu_{12} + n\nu_{12}^2)}{m(1+\nu)} \tag{9a}$$

$$\mu = \frac{E_2}{2(1+\nu)} \tag{9b}$$

$$\alpha = \mu - G_{12} \tag{9c}$$

$$\beta = \frac{E_2\nu_{12}^2(1-n)}{4m(1+\nu)} \tag{9d}$$

$$\gamma = \frac{E_1(1-\nu_{12})}{8m} - \frac{\lambda + 2\mu}{8} + \frac{\alpha}{2} - \beta \tag{9e}$$

$$m = 1 - \nu - 2n\nu_{12}^2 \tag{9f}$$

$$n = \frac{E_1}{E_2} \tag{9g}$$

The Cauchy stress tensor can also now be obtained by pushing forward the Piola-Kirchhoff stress tensor with the deformation gradient:

$$\sigma^e = \frac{2}{J}(\boldsymbol{F} \cdot \frac{\partial \psi^e}{\partial \boldsymbol{C}} \cdot \boldsymbol{F}^T) \tag{10}$$

. The stiffness matrix can be derived by integrating equation 7 which yields equation 11:

$$\begin{aligned}\widehat{\boldsymbol{C}}_{\boldsymbol{IJKL}} = {} & \lambda(2J-1)\boldsymbol{I}_{\boldsymbol{ij}}\boldsymbol{I}_{\boldsymbol{kl}} + \frac{2}{J}[\mu - \lambda J(2J-1)]\delta_{ik}\delta_{jl} + 8\gamma \boldsymbol{a}_{\boldsymbol{i}}\boldsymbol{a}_{\boldsymbol{j}}\boldsymbol{a}_{\boldsymbol{k}}\boldsymbol{a}_{\boldsymbol{l}} + 4\beta\left(\boldsymbol{a}_{\boldsymbol{i}}\boldsymbol{a}_{\boldsymbol{j}}\boldsymbol{I}_{\boldsymbol{kl}} + \boldsymbol{I}_{\boldsymbol{ij}}\boldsymbol{a}_{\boldsymbol{k}}\boldsymbol{a}_{\boldsymbol{l}}\right) \\ & - \alpha(\boldsymbol{a}_{\boldsymbol{i}}\boldsymbol{a}_{\boldsymbol{l}}\boldsymbol{b}_{\boldsymbol{jk}} + \boldsymbol{b}_{\boldsymbol{ik}}\boldsymbol{a}_{\boldsymbol{j}}\boldsymbol{a}_{\boldsymbol{l}}) - 4\beta(I_4 - 1)\delta_{ik}\delta_{jl}\end{aligned} \tag{11}$$

where **I** is the identity matrix. To ensure good convergence in a finite element program, the consistent Jacobian matrix needs to link the Kirchhoff stress to the rate of deformation [32]. This can be done with a push forward operation on $\widehat{\boldsymbol{C}}$ where the transformation is described in ref. [33] and [34].

$$\widehat{\boldsymbol{C}}^{\boldsymbol{e}}{}_{\boldsymbol{ijkl}} = \frac{1}{J} F_{iI} F_{jJ} F_{kK} F_{lL} \widehat{\boldsymbol{C}}_{\boldsymbol{IJKL}} + \frac{1}{2}\left(\delta_{kl}\boldsymbol{\sigma}_{\boldsymbol{ik}} + \delta_{ij}\boldsymbol{\sigma}_{\boldsymbol{kl}} + \delta_{kj}\boldsymbol{\sigma}_{\boldsymbol{il}} + \delta_{il}\boldsymbol{\sigma}_{\boldsymbol{kj}}\right) \tag{12}$$

CHAPTER 2

DEFECT ANALYSIS

Defects can cause resin rich areas and voids within the composite, which directly impacts the strength and fatigue behavior [35]. Much of these defects can be traced from the manufacturing of the composite such as the material orientation deviating during deposition [14]. Currently, the tradeoff of AFP's rapid manufacturing in a curved pattern is that the possibility of more fiber misalignment. In general, layup defects are inevitable when using automated manufacturing methods of composites. Images present in this chapter for the microscopy were taken with the Olympus with motorized XY stage and stitching capability and the CT-scans used a ZEISS Xradia 520 Versa 3D X-ray microscope. Micrographs of composites with induced defects, gaps, overlaps and folds, were taken.

2.1 Defects Resulting from Deposition Process: Fiber Tow Gaps and Overlaps

Materials can vary widely, and as a result the width of a tow used in AFP can also vary depending on the quality of the material. This can cause positive or negative spaces between the plies which results in gaps and overlaps in the composite structure respectively [36]. With the capability of rapidly changing the angle of a ply, tow steering in AFP structures commonly experience the these types of defects [24]. Gaps and overlaps during cure develop into waviness and fiber misalignment [13], [37]–[39]. Missing tows also allow for increased resin flow into the defects which creates pockets of resin rich regions [40]. Figure 3 depicts a composite with a resin rich pocket and a ply which was transversely squeezed due to the gap. Overlapping plies have also been shown to cause voids within the composite as shown in Figure 4. The micrograph of a deposited gap region after consolidation depicts a lack of fiber in the area and in plane waviness in the ply which could initiate failure (fig. 5). These effects influence the microstructure and influence the geometry of the resulting composite structure [41]. Gaps and overlaps can be reduced by narrowing the fiber width but at the cost of decreasing the deposition rate [14].

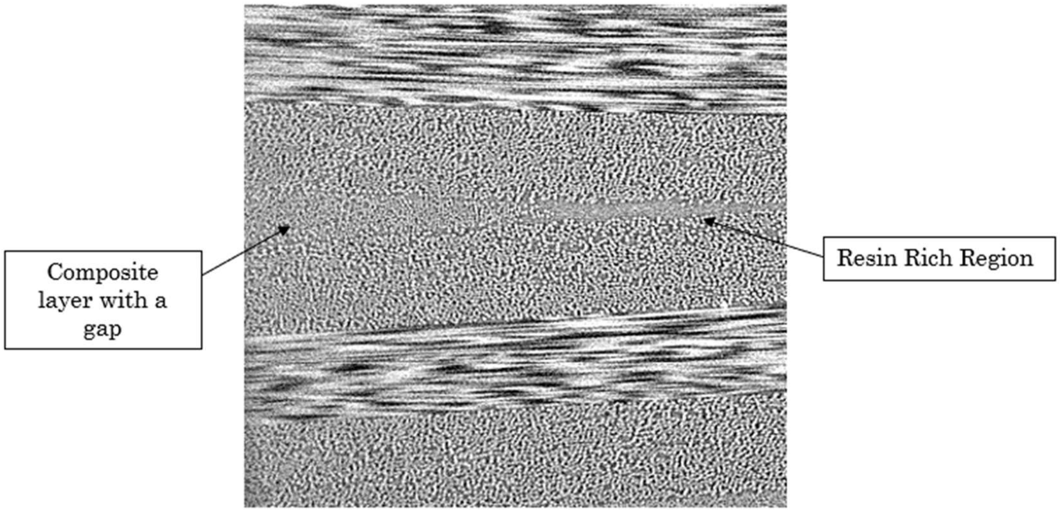

Figure 3. CT scan of a resin rich region made from a gap in the layup

Research has been done on the effects of gaps and overlaps of composite structures which shows gaps and overlaps are found to affect compressive strength of laminates [42]. Resin rich regions within gaps promotes failure in the area to occur due to localized stresses [35]. With proven reductions in material properties it is important to identify gaps and overlaps and determine the parameters that could minimize their impact on manufactured composites.

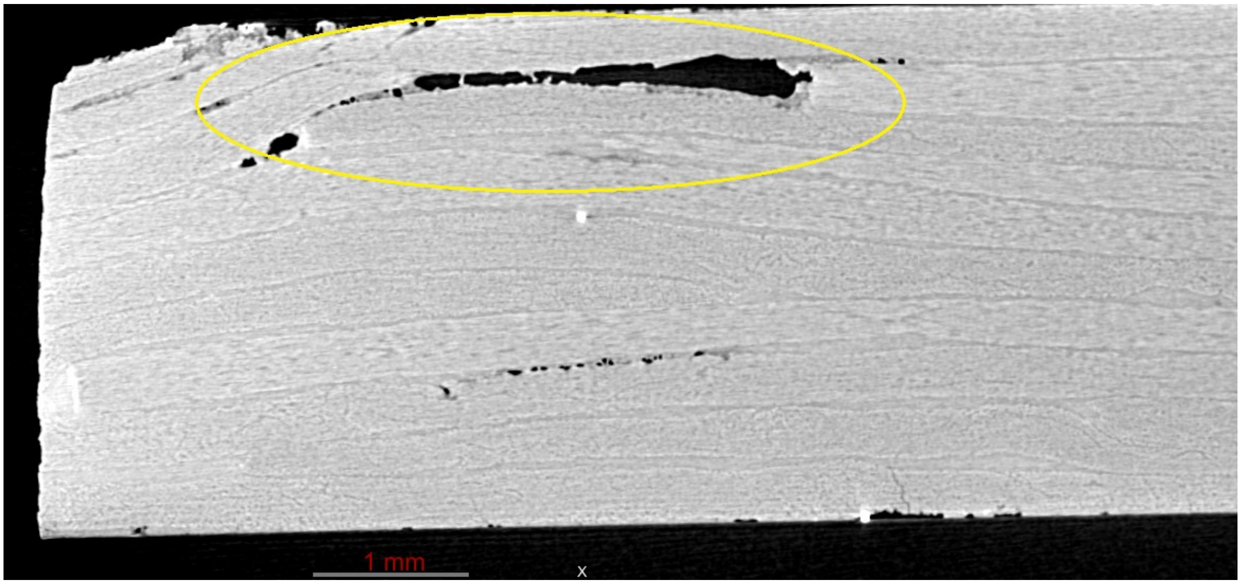

Figure 4. CT-scan of overlapping plies that causing voids in the composite.

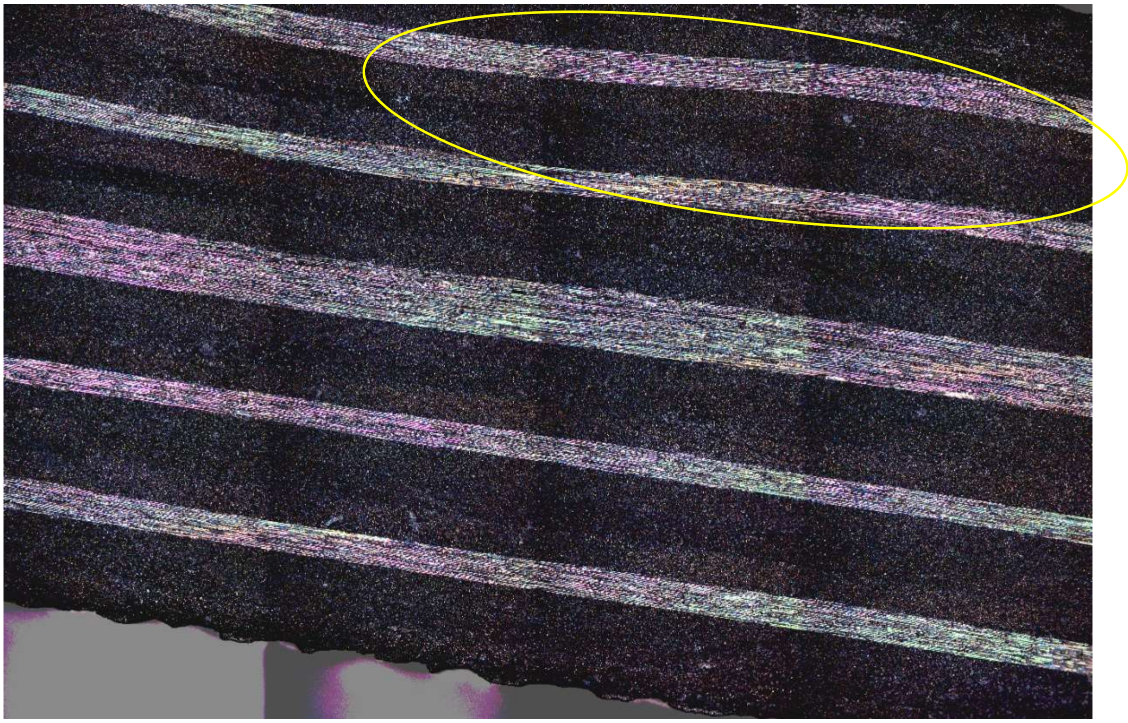

Figure 5. A micrograph of a gap in an AFP made composite which shows voids and a highlight to the 0° ply bending because of the fold.

2.2 Fiber Tow Folds

When a composite fails to adhere onto a surface, the tow may fold out of plane. This results in undulation in the tow [43]. More importantly, the defect can be caused by fiber steering, which is a prominent feature in AFP. Due to the nature of a curvature, parts of the composite may experience stretching or compressing which cause the tow to fold or wrinkle [45]. Research also states that the material stiffness plays a role in the formation of this defect [45]. Folds obstructs other plies and can create neighboring resin rich areas, form voids and ply thickness variations (fig. 6) and cause waviness within the fiber composite. These deformations are shown to be extensive, which shows the necessity to model such large deformations in process modeling. Several studies confirm that out-of-plane waviness decreases the strength and stiffness of fiber composites [46]–[49]. Guidelines for the turning radius to limit the curvature of the tow path with respect to specific material are available to prevent this defect [50]–[53]. However, with process modeling a more in-depth study into the optimization of other parameters is essential for the minimization of this defect.

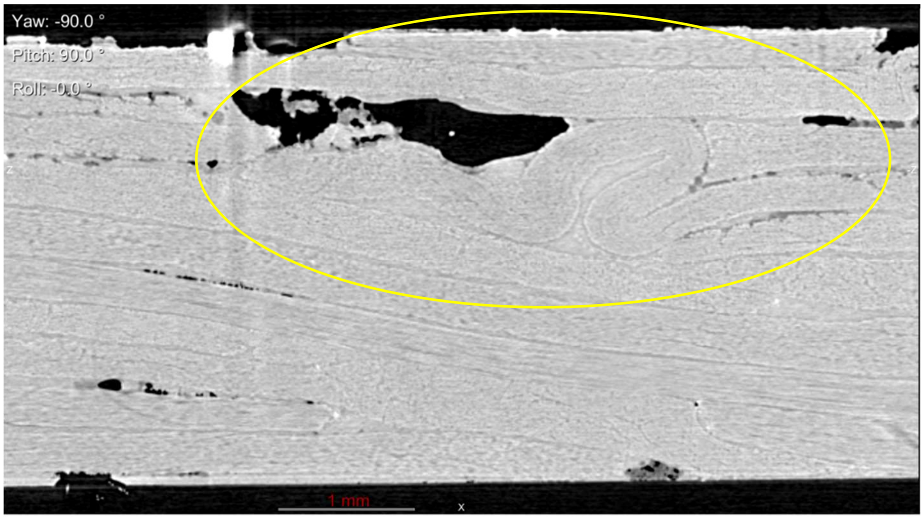

Figure 6. CT scan of a fold next to a void

CHAPTER 3

METHODOLOGY

3.1 Hyperelastic Compaction Model

The formation of defects in composite manufacturing is a problem that needs to be addressed for the certification of AFP made composites. Predicting defect formation in AFP composite is therefore necessary to optimize the manufacturing process. The proposed method for this approach is through FEA. The two distinctive but related works conducted are the modeling of residual stress deformation for a cylindrical shell made using AFP and the modeling of a hyperelastic model both of which was done through FEA. Residual stress occurs after the formation of the elastic and thermal properties and was conducted first. Some concepts were explored which will part of the second portion of this research. A thermo-chemical model and a hyperelastic model will be constructed which will be parts of a more comprehensive process modeling approach.

The process modeling of fiber reinforced composite for defect prediction needs several interconnected physical models to simulate the heat and consolidation of a thermoset (Figure 7~~Figure 7~~). The current work consists of the thermo-chemical model and the hyperelastic component of the consolidation model. The two models were made to work independently from one another to ensure that both can be analyzed separately or coupled together in a single process. Currently the coupling only includes the temperature which is used to derive the homogenized elastic properties for the hyperelastic model.

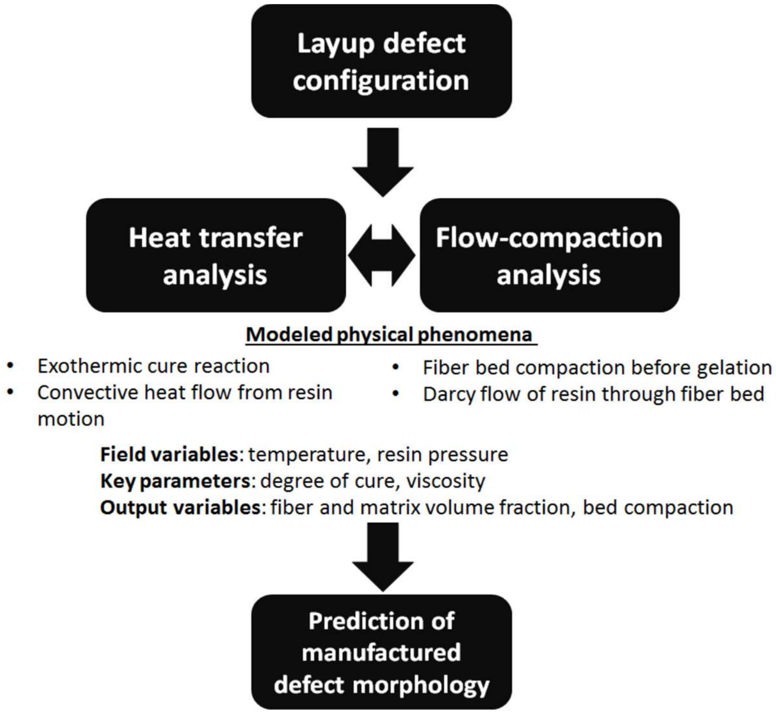

Figure 7. Coupled compaction and heat transfer analysis for predicting defects on AFP manufactured composites

3.1.1 Thermo-Chemical Cure Kinetics Model

To validate the thermo-chemical component of the visco-hyperelastic model, a prototype was created in Abaqus with a custom subroutine in UMATHT. The analysis is a simple experiment to test whether the proposed model can simulate the exothermic reaction of the curing process and properly model the cure kinetics. The model was a simple 20 mm x 3.0 mm x 20 mm block of a unidirectional carbon fiber composite (Figure 8~~Figure 8~~) with conductivity of 4.9 $W \cdot m^{-1} \cdot K^{-1}$ in the fiber direction and 0.58 $W \cdot m^{-1} \cdot K^{-1}$ in the fiber direction. The specific heat of the carbon fiber is 904.3 $J \cdot kg^{-1} \cdot K^{-1}$. The model is a transient heat transfer model that simulate the convective heat loading inside an autoclave. The density of the material was 1520 kg/ m^{-3} with a fiber volume fraction of 0.55.

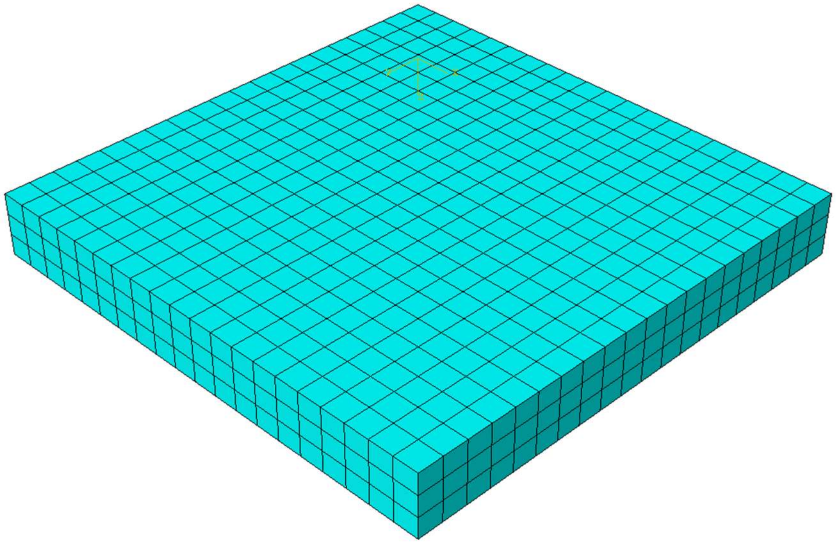

Figure 8. Thermo-chemical model of a carbon fiber composite

The composite was set to an initial temperature of 291 K, and a maximum thermal load of 450 K was added to the model through a surface film condition with a film coefficient of 50 W·m^{-2}·K^{-1} The temperature was applied in a classical double hold cure cycle up (Figure 9~~Figure 9~~) spanning 315 minutes with a step size of one second. The cure kinetics used is the aforementioned modified Arrhenius model (Eq. 2) with constants found in ref. [54]. The heat of reaction as function of the degree of cure was directly added as internal energy with a total value of 474.9 kJ. The cross-linking reaction of the thermoset is expected to produce exothermic heat. The low conductivity of the composite will create a concentrated temperature in the middle of the composite as the reaction occurs.

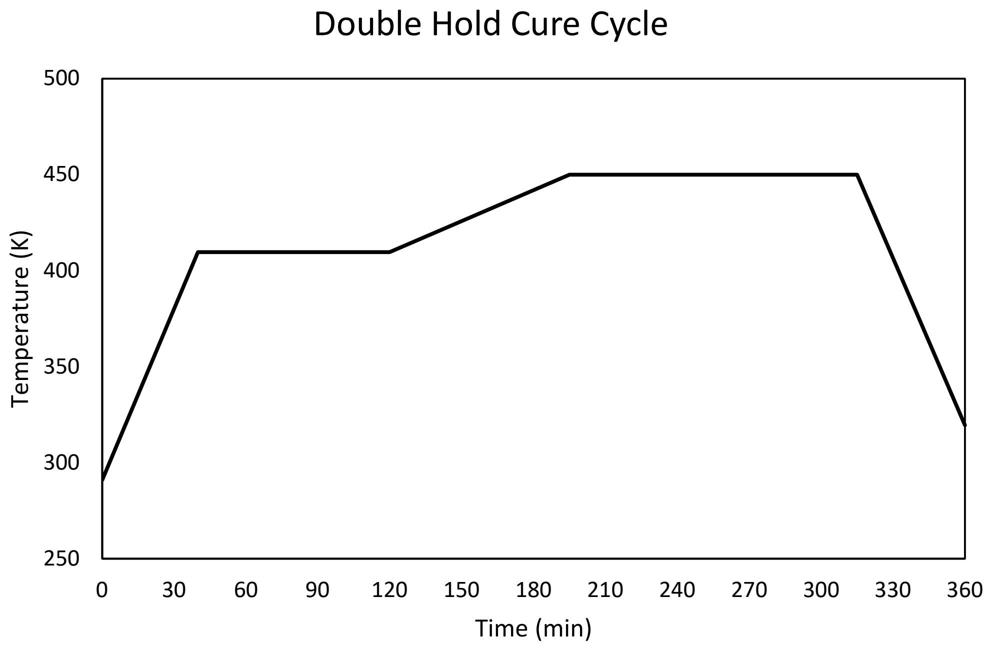

Figure 9. The applied temperature over time of a double hold cure cycle

3.1.2 Hyperelastic Compaction Model

The initial step to a functional visco-hyperelastic model involves modeling the hyperelastic component, which is attributed to fiber bed compaction. As previously discussed, the elastic model is a constitutive equation that involves invariants of the Cauchy-Green deformation tensor. As an initial simulation for the modeling of the hyperelastic component a simple model with 40 hexahedral elements which has three 0.01 mm thick layer and a length and width of 0.04 mm. A gap was modeled in the center which was 0.01 mm thick, with a length and width of 0.02 mm x 0.04 mm (fig. 10). The density of the material is 1590 kg/m^3.

To determine the properties of the resin, a function of the glass transition temperature, and the degree of cur was utilized. The glass transition temperature was calculated using Dibenedetto's equation [55]. The elastic modulus was then calculated with the isothermal and cooling equations found in ref. [56] using an equation with the capability to transition between the isothermal phase and the cooling phase. The properties of the composite were then derived using Schapery's homogenization and carbon fiber were derived from literature [57], [58]. The Arrhenius model was used to calculate the degree of cure, which in turn was used to derive the glass transition temperature. The elastic properties of the matrix were calculated as a function of glass transition temperature and the degree of cure. With the fiber properties held as a constant, the properties of the matrix and the fibers are homogenized for the composite properties using the equations in Appendix 1.

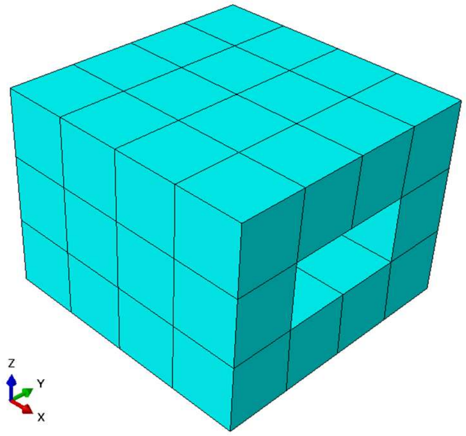

Figure 10. The FEA model for the elastic component

The analysis was done in Abaqus with a UMAT and UMATHT subroutine. UMAT was used to calculate the stiffness matrix for the analysis of the equation and UMATHT was used for the calculation of the heat transfer, exothermic heat reaction, temperature, and the degree of cure. The same cure cycle was used as in the heat transfer model (Fig. 11). UFIELD and USDFLD were used to supply the material orientation vector for each integration point which is used to rotate the stiffness matrix appropriately. For stability, the maximum time increment used was 0.25 seconds and a damping factor of 0.2 was used. Furthermore, the Cauchy-Stress tensor was modified as equation 13.

$$\bar{C} = C(J^{-\frac{2}{3}}) \tag{13}$$

where $\bar{C}$ and the J is the Jacobian of the Cauchy-Stress tensor. This is to analyze only the volume preserving contribution of the tensor. The pressure was ramped from ambient 101 kPa to 434.7 kPa and then the pressure steadily increases from 434.7 kPa to 483 kPa for 215 minutes. The boundary conditions and the measurements of the model are shown in Figure 16. The bottom has Z-direction boundary conditions, and Y-direction boundary conditions on the center of the composite are shown in the Y-Z plane of the picture. Symmetrical boundary conditions were applied to both planes facing the X-direction.

3.2 Residual Stress and Deformation Analysis

3.2.1 Digital Image Correlation

The thermal expansion properties of AFP manufactured unidirectional lamina were used to model the residual deformation in the AFP shell structure. Digital image correlation (DIC) provides a reliable and tested method to measure the strain due to thermal expansion in composites [26], [27] to use for the present study. The surface displacement and corresponding strain fields, as a result of unconstrained thermal expansion, are determined using the analysis. GOM correlate (GOM, Braunschweig, Germany) software was used to measure the thermally induced strain on the composite surface.

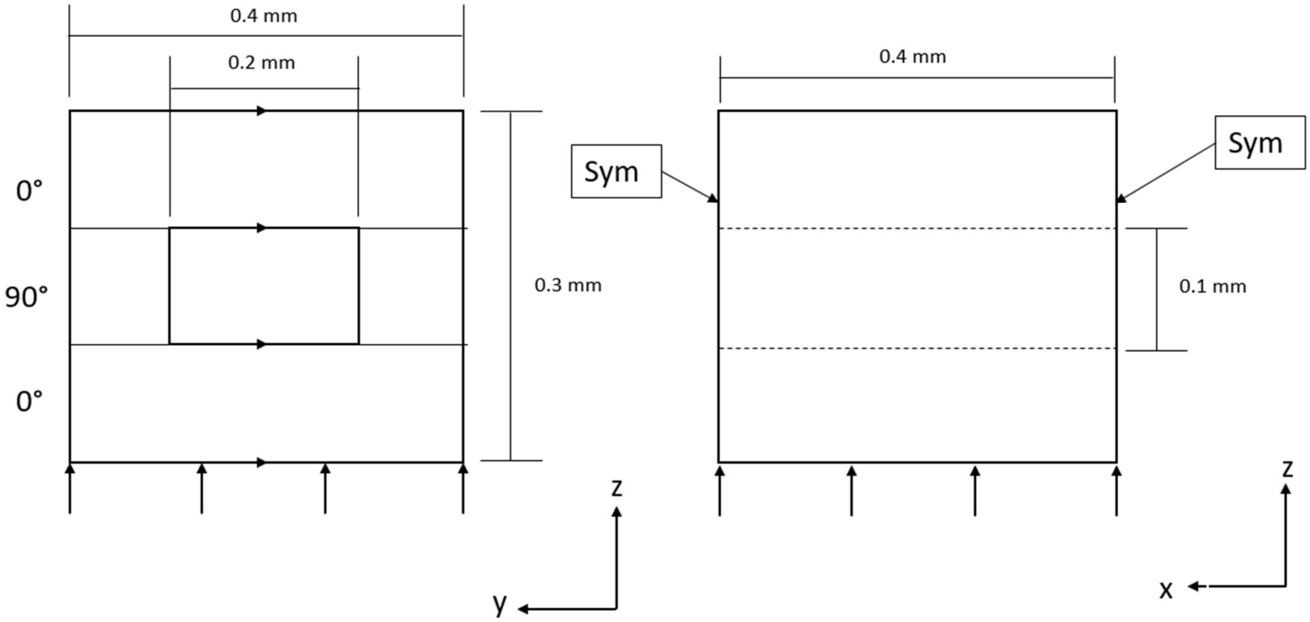

Figure 11. The Boundary conditions and the measurements of the FEA model

The goal of this research is to investigate the cooling of AFP made composite in complex structures through simple FEA models. An experimental part was conducted for the properties of the model. The resulting morphology of the composite was measured and compared to out-of-roundness data derived from experimental CMM measurement

The material used in the present work was Hexply® IM7/8552 prepreg with low tack behavior, which is specifically developed for the AFP process. Rectangular samples of cured unidirectional composite with dimensions of 1.2 in. x 1.6 in. were used to analyze the thermal expansion. Each specimen was 24 plies (0.158 in.), for an average of 0.0066 in./ply. A Dino-Lite Edge 3.0 digital microscope was used to take pictures of the composite for DIC analysis during thermal heating. A long lens cap was used for low magnification pictures and care was taken to avoid light glare obscuring the view of the speckle pattern. The camera was calibrated to provide perpendicular orientation with respect to the plane of the sample, and the coordinate system was aligned for the measurement of thermal strain data in fiber and transverse to the fiber direction. Fig. 12 shows the experimental setup used for determining the coefficient of thermal expansion.

The speckle pattern, shown in Fig. 13a, was painted by spraying the surface of the sample at an angle with white acrylic paint to contrast the dark colored composite surface. A thermocouple was placed next to the sample and was used to measure the temperature of composite, while the images for the DIC analysis were recorded using the digital microscope. A glass cover was placed over the sample to create a more uniform temperature around the sample.

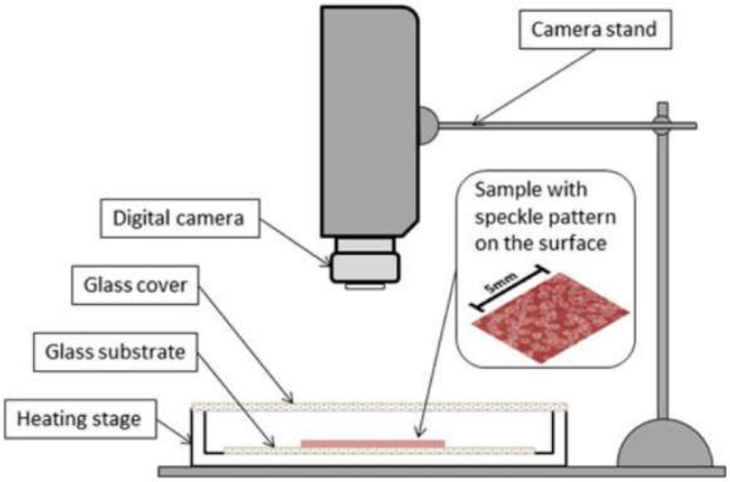

Figure 12. Schematics of DIC setup

The references for the DIC analyses were taken at room temperature of 68º F. The experiment was initiated by ramping the temperature to 86º F and then increasing the temperature in 36º F increments up to 302º F, and at smaller intervals of 18º F up to 367º F which the strain profile is shown at Fig 13b. The sample was heated to each isothermal condition in the considered temperature range and allowed to reach thermal equilibrium for 10 minutes. Six trials were done, which were three repetitions of two samples each of the same material. The area of interest within the sample was analyzed by determining the thermal strain in principal material directions for each isothermal temperature condition [59]–[61]

3.2.2 CTE Analysis

The laminate was assumed to be transversely isotropic with principal directions given by longitudinal (fiber) and a transverse direction. Expectedly, the strain exhibited anisotropic properties with the transverse direction showing a higher magnitude than the longitudinal direction due to epoxy matrix dominated properties [62], [63]. Two samples were used for the measurement, with three tests conducted on each one. CTE was measured by calculating the slope with a simple linear regression of temperature versus strain plots which gives the thermal strain, ${\Delta\varepsilon_i}^{TH}$:

$$ {\Delta\varepsilon_i}^{TH} = CTE \text{ x } \Delta T \tag{14} $$

where $i = 1,2$ denote fiber and transvers to the fiber directions respectively.

The CTE in fiber direction ranged from a minimum of -1x10^{-6}/°F to a maximum of 2x10^{-6}/°F with an average and standard deviation of 0.75 ± 0.943 x10^{-6}/°F. The transverse CTE direction was recorded with a range from 16x10^{-6}/°F to 24x10^{-6} /°F with an average of 20.6 ± 4.49x10^{-6}/°F (fig. 13). The experimentally measured thermal expansion coefficients were determined below the glass transition temperature, which corresponds to the temperature range for cooling regime during the manufacturing cycle and therefore these CTE values were used for the FEA modeling discussed in the following section.

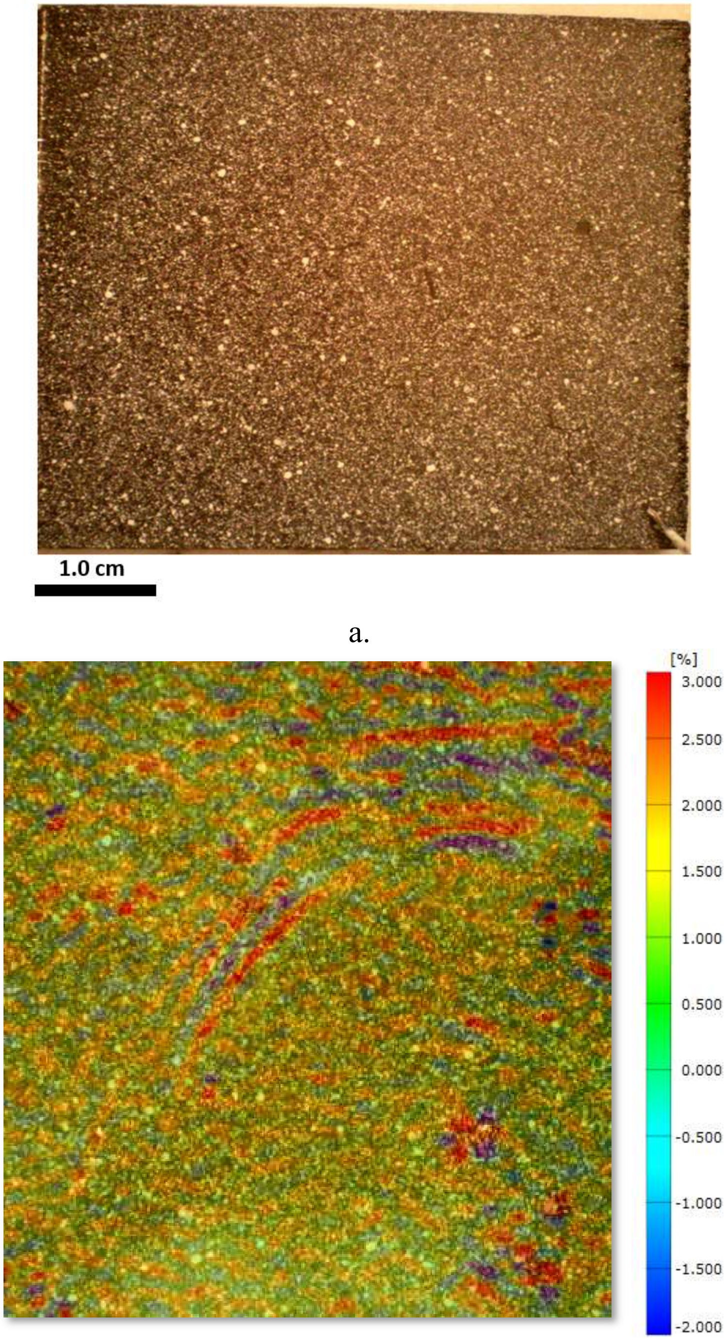

a.

b.

Figure 13. a. Speckle pattern for Digital Image Correlation analysis b. Strain Profile at 367 º F

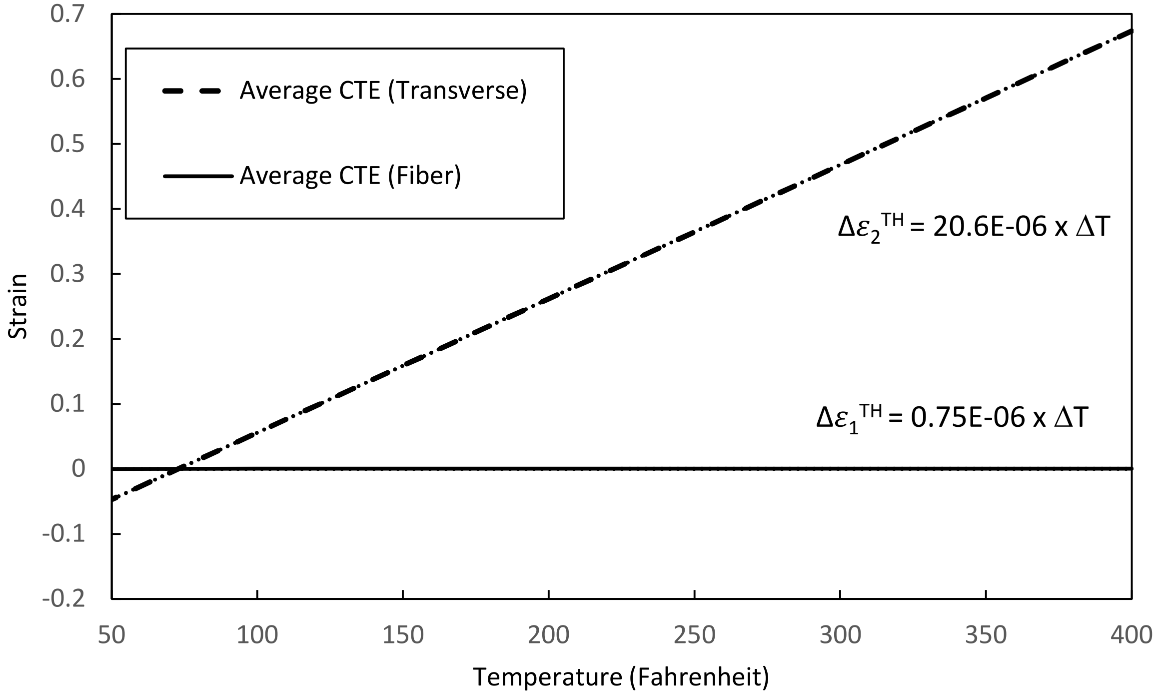

Figure 14. CTE in fiber and transverse directions

3.2.3 Self-Consistent Field Micromechanical Relations

A change in temperature of a composite consequently affects the mechanical properties leading to material softening with temperature [16], [64], [65]. To study the role of composite softening with increased temperature on the residual deformation during the cooldown stage, the lamina properties were calculated as a function of temperature using the self-consistent micromechanical model for elastic properties and Schapery's homogenization for the CTE [66], [67]. Temperature-dependent properties were calculated assuming constant carbon fiber mechanical properties and epoxy matrix moduli, which decrease linearly with increased temperature below the glass transition [68] as shown in Table 1, with corresponding CTEs for fiber and matrix. The carbon fiber properties were selected to agree with the room temperature lamina moduli reported in Ref. [69], [70] then the lamina properties were calculated as a function of temperature using the micromechanical model.

The predicted change in lamina properties showed that fiber dominated properties were not affected by the temperature, namely values for ν_{12} and E_1 which remained relatively constant, changing about 0.1%, for the temperature range. The value that exhibited the most change is G_{12} which decreased about 20% from its room temperature value. The CTE in the fiber direction shows a significant change, however the value of the coefficient is rather small, as it only changes by a magnitude of $0.3\text{x}10^{-6}$/F°. Unlike the other properties, the transverse CTE displayed an increase of 0.1%. This indicates that lamina CTE is mostly unaffected by the change of temperature unlike the elastic mechanical properties.

Table 1. Carbon Fiber Properties

Material constants	**Fiber Properties**	**Matrix Properties**		**Lamina properties**	
		Room Temperature	**Properties at 354 °F**	**Room Temperature**	**Properties at 354 °F**
Longitudinal modulus (Msi), E_1	29.7	0.435 (isotropic)	0.287 (isotropic)	19.48	19.43
Transverse modulus (Msi), E_2	2.17			1.36	1.04
In-plane shear modulus (Msi), G_{12}	3.77	0.167 (isotropic)	.105 (isotropic)	0.756	0.528
Out-of-plane shear modulus (Msi), G_{23}	8.63			0.583	0.441
Major Poisson's ratio, ν_{12}	0.26	0.30		0.347	0.346
Longitudinal CTE (10^{-6}/F°), α_1	-0.5	22.78 (isotropic)		0.75	0.90
Transverse CTE (10^{-6}/F°), α_2	8.3			20.05	20.05

3.2.4 Finite Element Analysis and Residual Deformation Measurement

Residual stress analysis was done with consideration to Wu's [6] AFP composite shell. The two shells were modeled and labeled Shell A and Shell B, with and without overlaps, respectively. The finite element models are modified after White's et al. [20] study that considered buckling and post-buckling analysis of these shells. Therefore, the established homogenized lamina properties were used in the present study as well. A four-node shell finite element formulation was employed, with the variable fiber orientation, corresponding to the stacking sequence produced during the deposition of AFP tows [20], [71]. The composite structure model consists of shell elements that consist of 51 sections for Shell A and 174 different sections for Shell B with unique layups, orientations, and thicknesses. This results in a piecewise stiffness matrix for the model to simulate the unique layup patterns in the composite structure.

The shell model included as manufactured configurations of the AFP shell (fig. 15) which had 7 in. removed prior to compressive testing [20]. The radius of the mandrel used in the manufacturing of the composite shells had the nominal radius of 8.133 in. [5] and is assumed to be made of steel with a CTE of $7.6\text{x}10^{-6}$/°F. The increasing in temperature from 73.4 °F to 352.4 °F expands the mandrel about 0.015 in. to 8.15 in. radius. The study observes the effects of residual stress due to cooling in complex AFP layup using composite shells elements in FEA. The mandrel expansion radius was added to the finite element model to account for the tool expansion at the initial temperature. The FEA program Abaqus Unified FEA (Dassault Systems, Vélizy-Villacoublay, France) was used to analyze the residual deformations during the cool down stage.

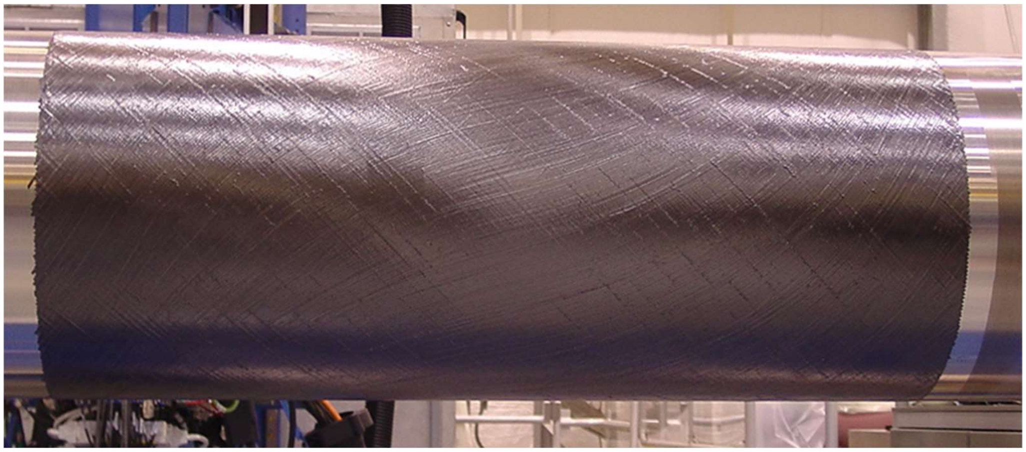

Figure 15. As-Manufactured AFP composite shell on the tool mandrel [5]

This work explores the effect of the layup configuration, produced due to steered pattern in AFP manufacturing, on thermally induced stressed during the cool-down stage. The laminates are modeled using shell finite elements that mimic the nominal layup sequence during AFP deposition stage. Naturally, due to differences in the deposition between the case with and without tow overlaps, the local thickness in the physical cylinders is not uniform. This is especially in the case of the overlapping tows that produce much thicker crown and keel. The variation in the thickness for the case of no fiber tow overlap is significantly smaller, as discussed in the subsequent sections. The effect of non-uniform thickness is considered in the simplifying shell formulation.

Eight models in total were ran to test various conditions, namely geometric linearity/non-linearity, constant/temperature dependent lamina properties, and shell geometry with or without overlaps. A uniform temperature field of 352.4º F was initialized for the model and lowered to 73.4º F to simulate cooling during manufacturing. A cylindrical coordinate system is used to analyze the out-of-roundness residual deformation patterns.

3.2.5 Post Processing

An algorithm developed by the European Association of National Metrology (EURAMET) Institute was used to find the best fit cylinder for the deformed shells. The least squares method was used to minimize the squares of difference in radial distance between the coordinates of the deformed shell and the best fit cylinder (eq. 15),

$$\begin{gathered}\{(x,y,z),(a,b,c),r\}\ minimize \sum_{i=1^m} d_i^2\,; \\ d_i = (x_i,y_i,z_i) - r((x,y,z),(a,b,c))\end{gathered} \tag{15}$$

where (x_i, y_i, z_i) are the coordinates of the deformed configuration, r is the radius of the best fit cylinder, with orientation defined by coordinates *((x, y, z), (a, b, c))*. EUROMETROS's function implements Least Square Fit Cylinder routine and outputs the parameters of the fitted cylinder. Fig. 16a shows the radial deformation of the shell due to cooling. Using the best fit cylinder analysis, the out-of-roundness is calculated, which is the difference between the coordinates of the deformed configuration to the fitted cylinder (Fig. 16b). These calculations are performed using MATLAB (Mathworks, Natick, MA, United States).

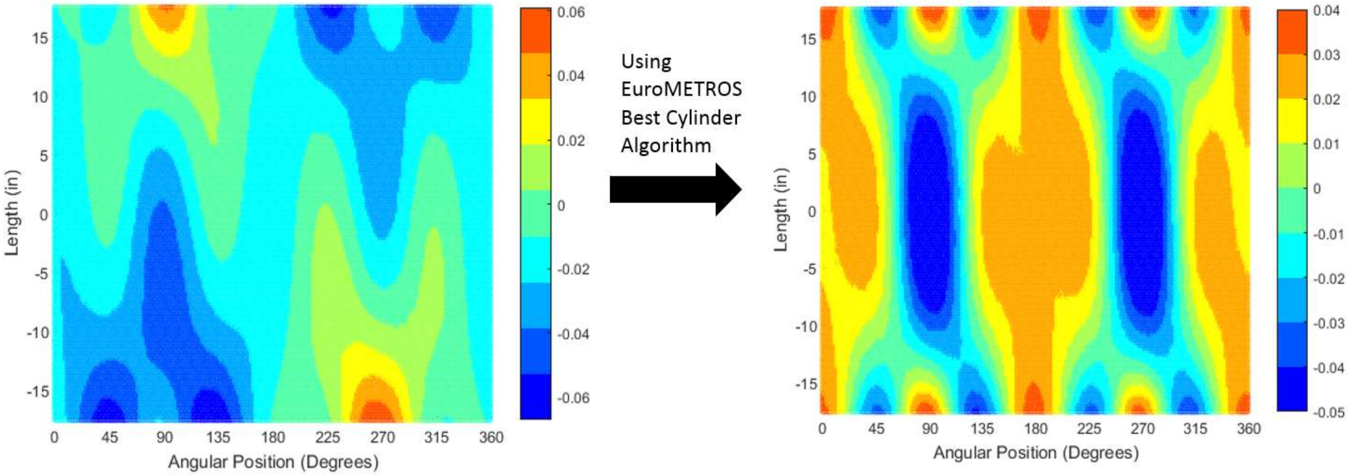

a. b.

Figure 16. *a. Deformed shell configuration; b. out-of-roundness plot*

CHAPTER 4

RESULTS

4.1 Thermo-Chemical Model

The results of the modeling show a functional model to simulate the heat transfer throughout the material. The center temperature, total heat of reaction, and degree of cure were measured. The plot of the degree of cure was probed at the center of the model (Fig. 17) follows a curve commonly found in thermoset composites [72]. The gelation process of the composite is marked by a rapid increase in the degree of cure from about 30 minutes to 58 minutes and a steady slope towards a fully developed resin.

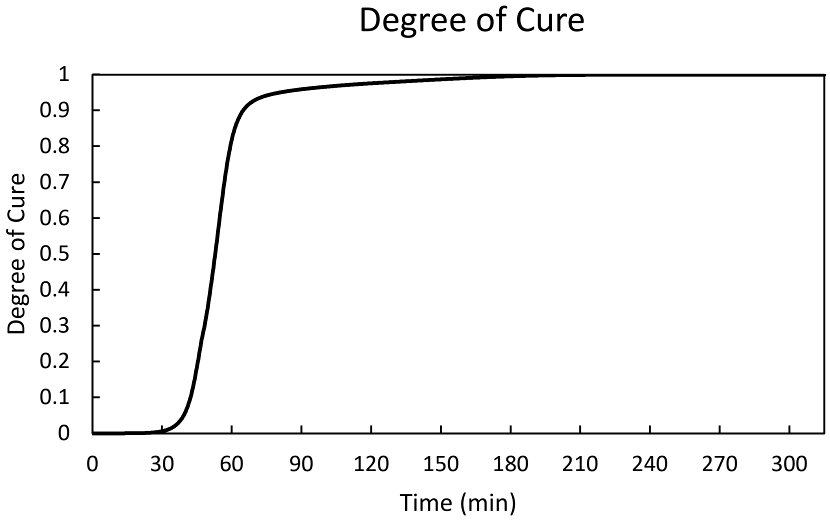

Figure 17. Degree of cure over time

As the composite cures, it undergoes an exothermic heat reaction due to the polymerization of the matrix, and the magnitude of heat released depends on the mass of the resin. Since carbon fiber composites have low conductivity, the heat from the reaction takes a relatively long time to dissipate through the material. As a result, the temperature at the center of the material surpasses the applied temperature (Fig. 18). The surface of the temperature also experiences the same phenomenon, but to a lesser extent. The exothermic reaction is most apparent in the first hold phase of composite curing (Fig. 19). The energy released by the exothermic reaction is also shown in the internal energy plot by the dip in the value at 60 minutes (Fig. 20). The maximum temperature in the model is 477 K, which is 6% hotter than the maximum applied temperature. This phenomenon is commonly observed during the curing of thermosets, and is especially apparent in thicker composites [73], [74].

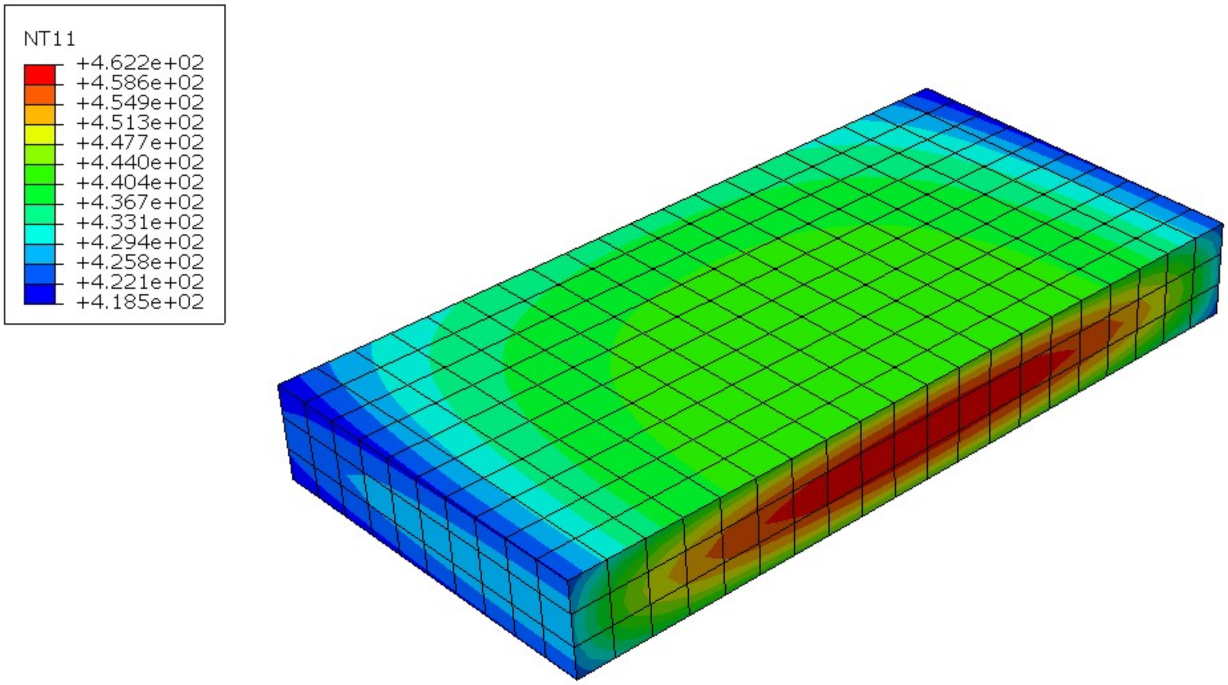

Figure 18. Exothermic reaction of the composite causing the center temperature to surpass the surface

The development of material properties is primarily dependent on the degree of cure during the curing phase of a composite. A change in temperature will also mean the formation of residual stress within the material [62]. Since material properties change with the gelation of the resin, it is necessary to evaluate the change of the degree of cure and the heat transfer through the material. Therefore, it was necessary to construct a preliminary thermo-chemical simulation as the base of the process model.

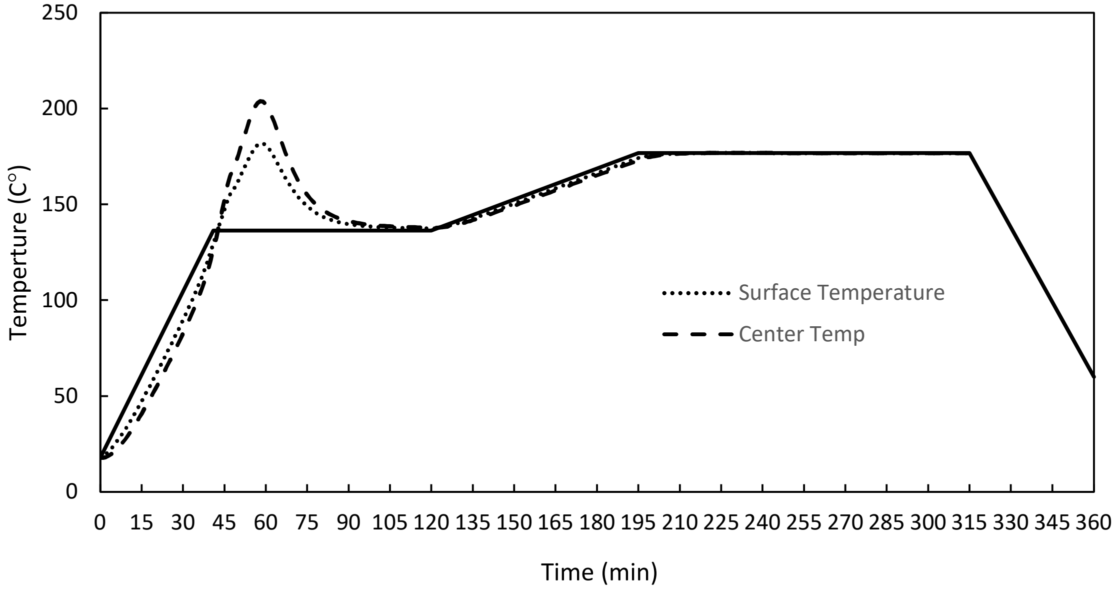

Figure 19. A plot displaying the exothermic reaction with applied and center temperature

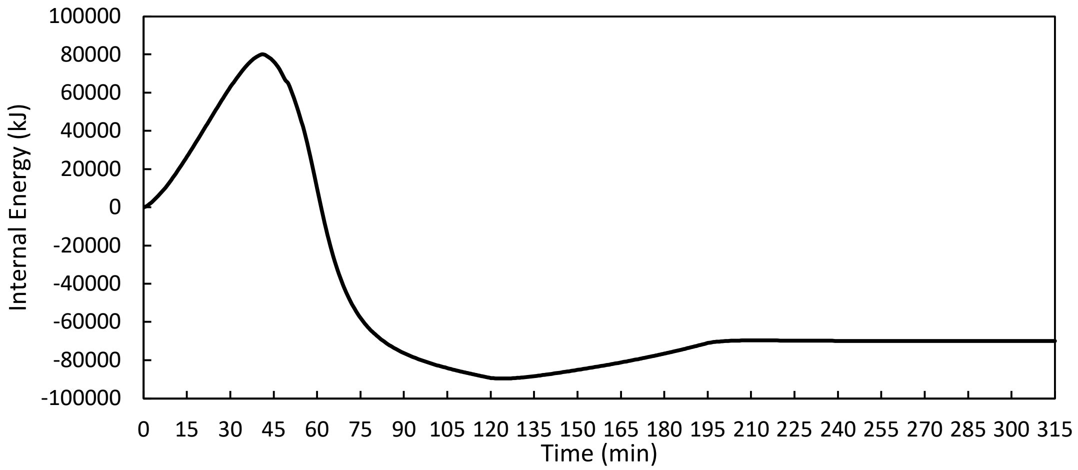

Figure 20. Internal energy plot showing released from the exothermic reaction

4.2 Elastic Compaction Model

The thermo-chemical analysis of hyperelastic model displays different results from the previous model due to differing geometry. Since the temperature and the rate of the temperature is constant throughout due to it being a thinner composite compared to the previous, there was no heat flux present in the model. The exothermic reaction of the composite was not enough to make a significant difference in applied and nodal temperatures since there was less mass in comparison to the thermo-chemical model test. However, it is the same thermo-chemical model used in the previous section which proved to adequately simulate heat transfer with an exothermic reaction. The curve of the degree of cure shows a curve with a discontinuity at 60 minutes that corresponds directly to the hold phases of the cure cycle (Fig. 21).

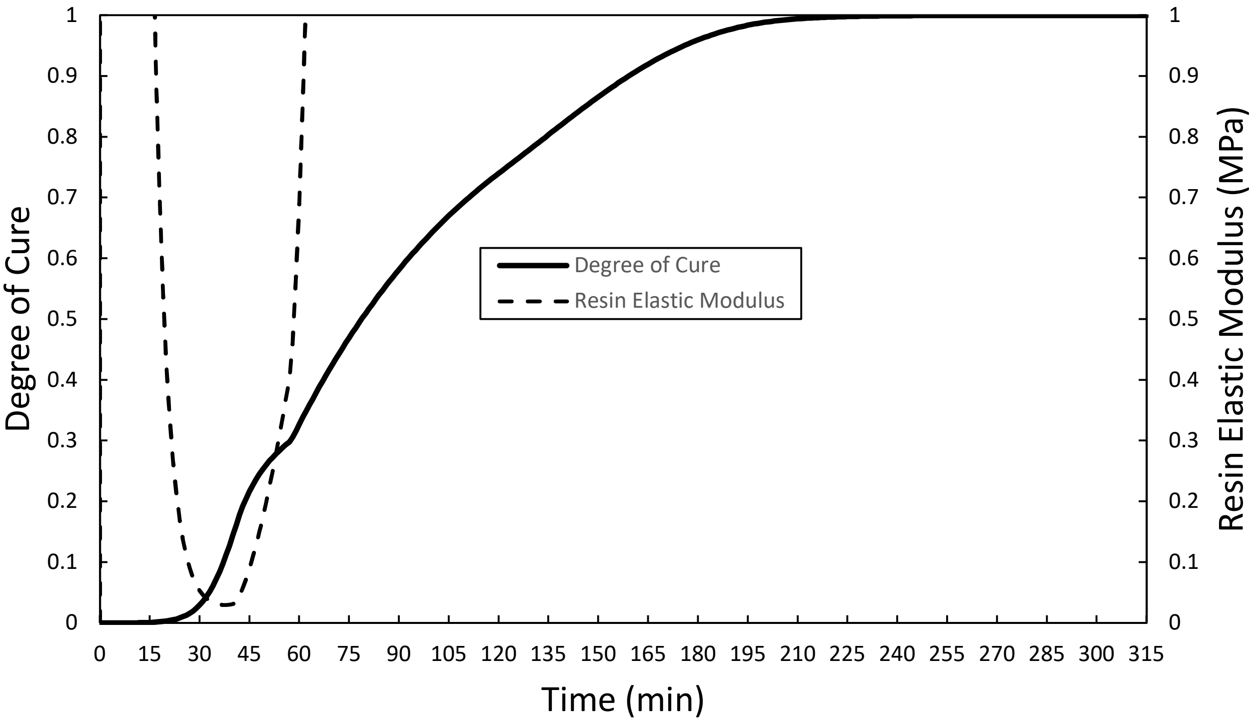

Figure 21. Degree of Cure curve of the elastic model.

The development of the elastic modulus of the resin is shown in Fig. 21. During the initial ramp of the temperature and pressure, the modulus is shown to be relatively low. However, when the resin begins to cure, the modulus is shown to increase logarithmically coinciding with the rapidly increasing degree of cure. A steep increase in the modulus coincides with the gelation of the resin. The development of the composite properties was governed by the changing resin properties. Most of the properties follow the trend of the resin modulus, with the exception of the poison’s ratio and the homogenized longitudinal elastic modulus where their values remain relatively constant which can be attributed to the Poisson’s ratio and the longitudinal modulus being mostly fiber dominated. The normalized elastic properties are shown in Figure 22 with the horizontal line following the X-axis being the Poisson’s ratio and the longitudinal elastic modulus.

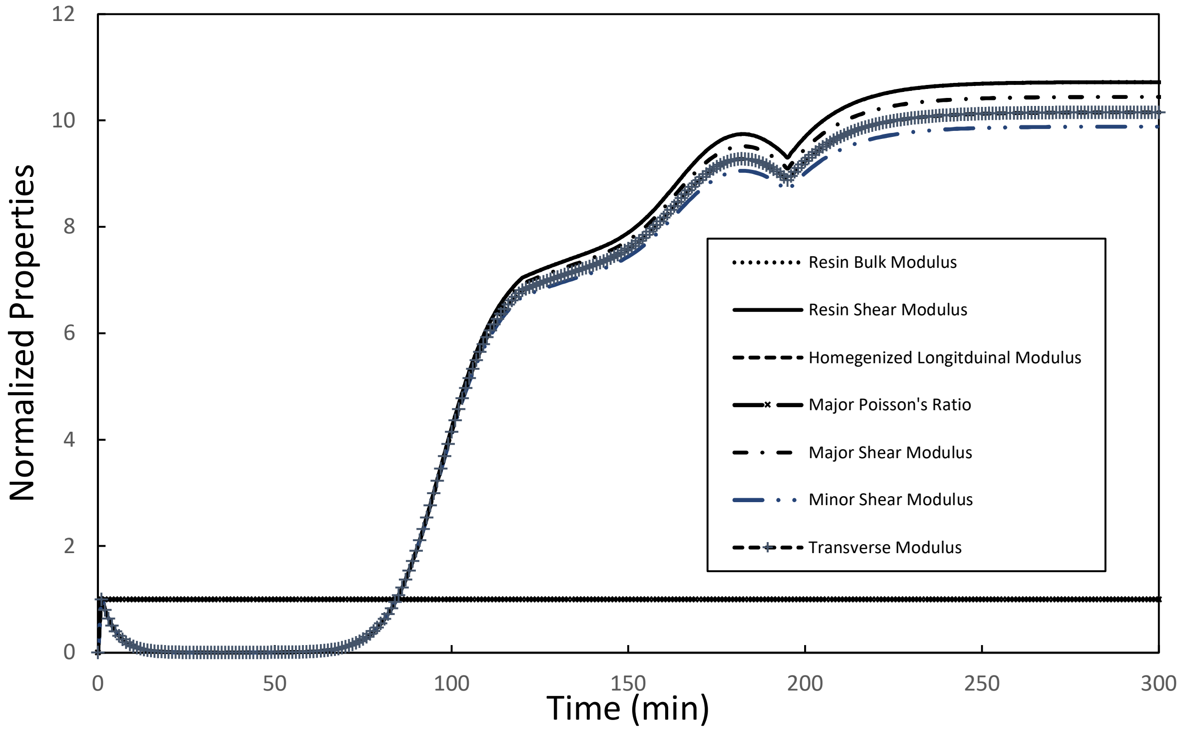

Figure 22. Normalized temperature dependent properties over time

For conventions, the stacking sequence is the z-direction, the center ply is 90° with its fiber direction pointed at the X-direction and the top and bottom plies are 0° have their fibers pointed in the Y-direction. With the pressure being applied at the top surface of the composite, the model has expectedly collapsed inwards into the defect. The top, bottom, and sides of the surface of the defect is shown to have deformed inwards. The top surface of the composite has a concave shape while the bottom 0° has mostly compressed outwards. The sides of the 90° ply are shown to have slight transverse deformation however, most of the deformation is shown to have occurred within the defect. Figure 23 exhibits a magnified view of the deformation that has taken place in the composite. The y-directions' stresses show that its mostly concentrated on the 90° ply with the inside surface experience tensile forces and the outside surfaces experience compression (Fig. 24). This indicates that the pressure causes the ply to expand transversely. Most of the z-directions' stresses are also concentrated in the 90° ply with some at the centers of the 0° plies (Fig. 25). This shows that the compression of the model happens mostly in the center ply. The strains in Figure 26 shows that the 90° ply experiences both tensile and compressive strain while the 0° ply is all in tension. The strain in Z-direction is mostly straightforward, with the 0° ply showing tensile strain in the center, while the 90° is under compression (Fig. 27). The angle at the defect was analyzed and compared to the resin rich region of the defect shown in CT scans in the previous a section. Fig. 28 shows that both the model and the CT-scan exhibit a wedging behavior where the top and bottom plies bend inwards towards the defect. However, the unlike the CT-scan, the middle ply of the model does not expand transversely. This shows that the model needs proper contacts in between the plies instead of being modeled a single geometry. While it is a good foundation for a visco-hyperelastic model, more research and work are needed to fully explore the model behavior under different boundary conditions.

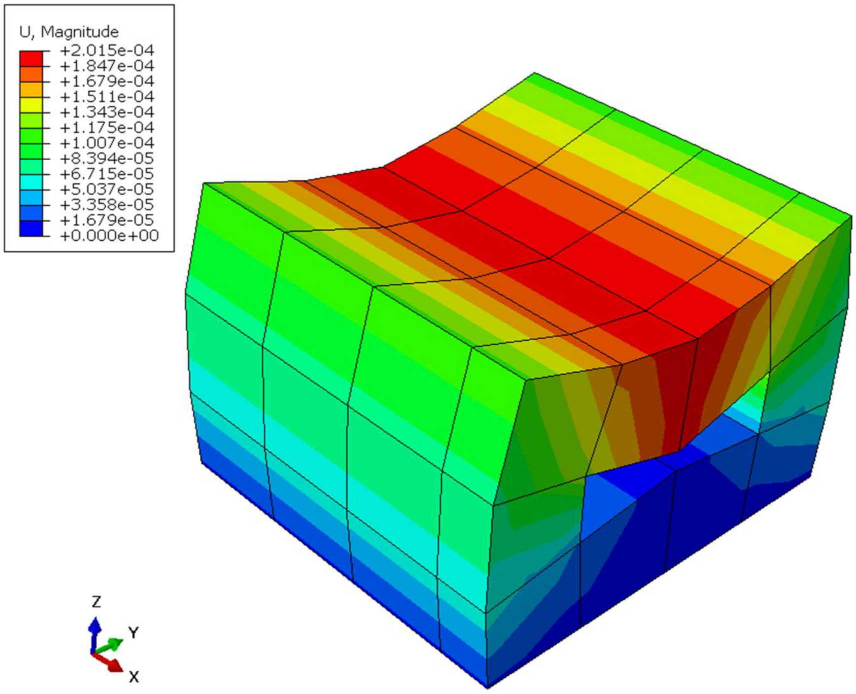

Figure 23. The deformed shape of the model

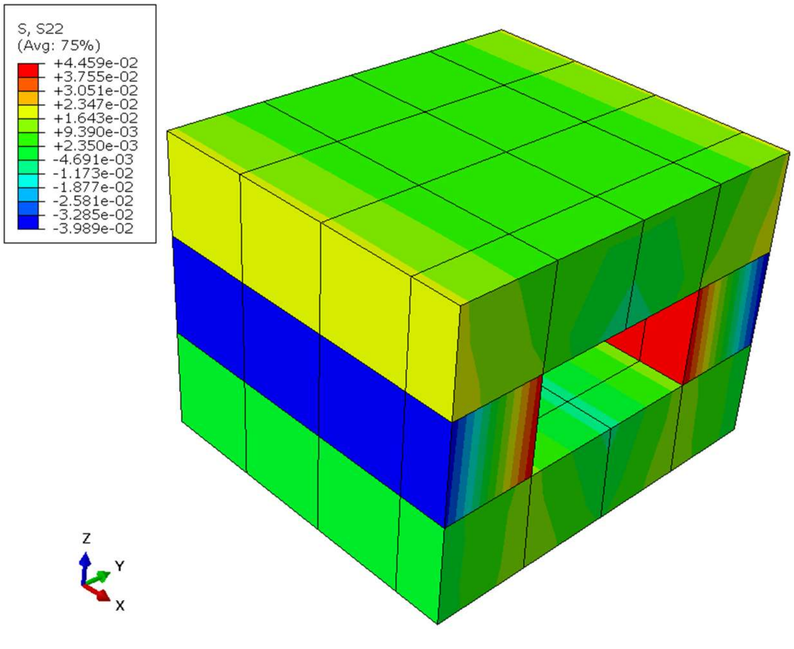

Figure 24. Stresses in the Y-direction

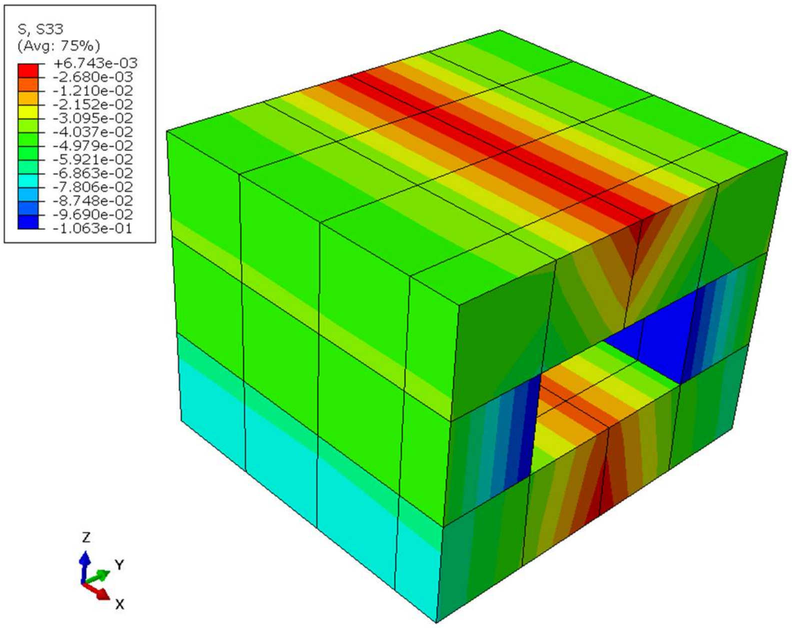

Figure 25. Stress in the Z-direction

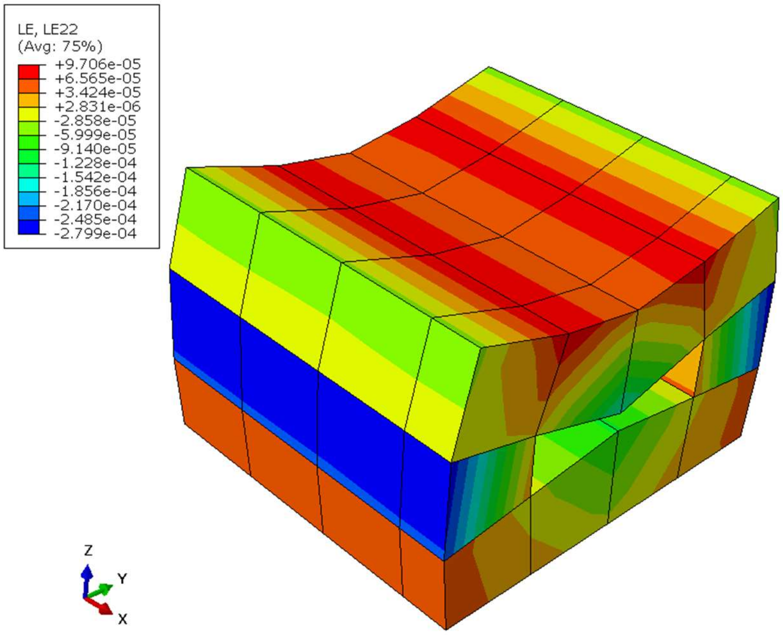

Figure 26. Strains in the Y-direction

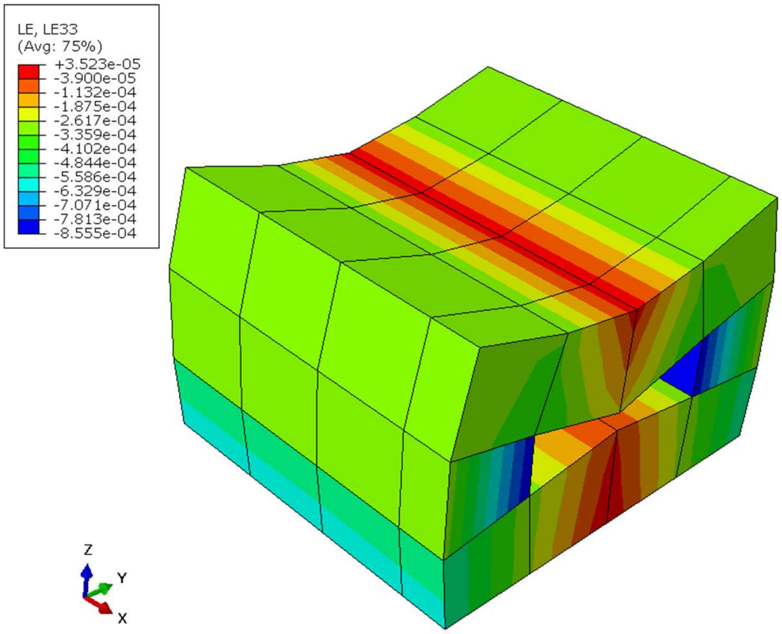

Figure 27. The Strains in the Z-direction

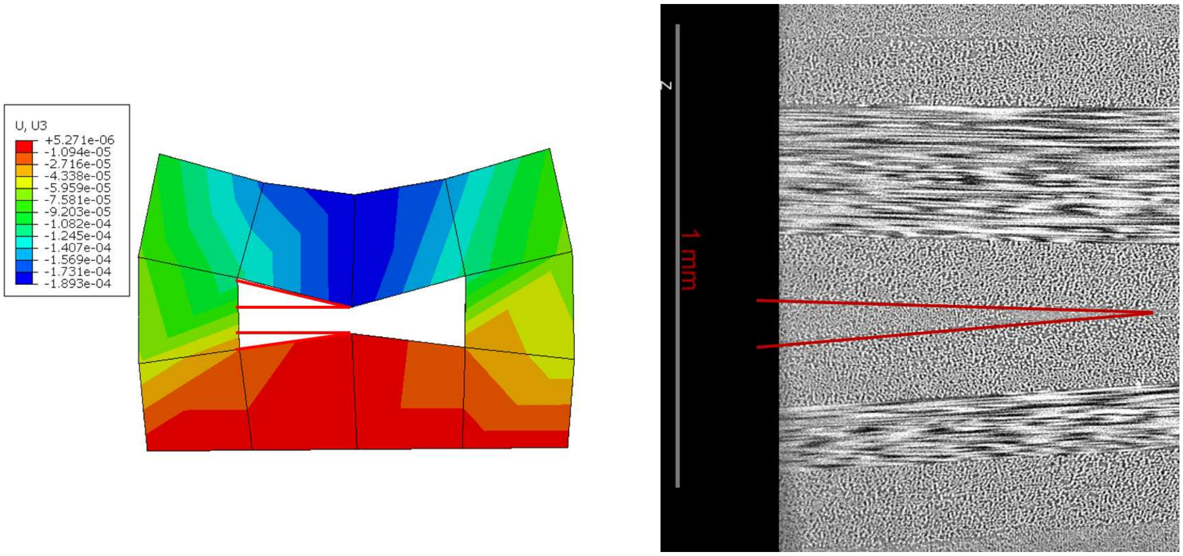

a. b.

Figure 28. A side by side comparison of the angles the two plies make in a defect region between a.) the finite element model and b.) the CT-scan

4.3 Residual Deformation Analysis

The experimental out-of-roundness data was used as the metric to compare to the results of different FEA analyses. The key cross-section areas of the cylinder were selected, namely at the outer edge, 8.75 in. away from the edge (denoted as "quarter") and the midpoint location (Fig. 29). The model used a pinned boundary condition at the crown location and a roller at the keel. These boundary conditions were chosen to avoid over-constraining the model due to anisotropic thermal contraction during the analysis. The best fit cylinder algorithm, which was used for the deformed shape analysis, can effectively account for the rigid body rotation, which is possible due to the applied boundary conditions.

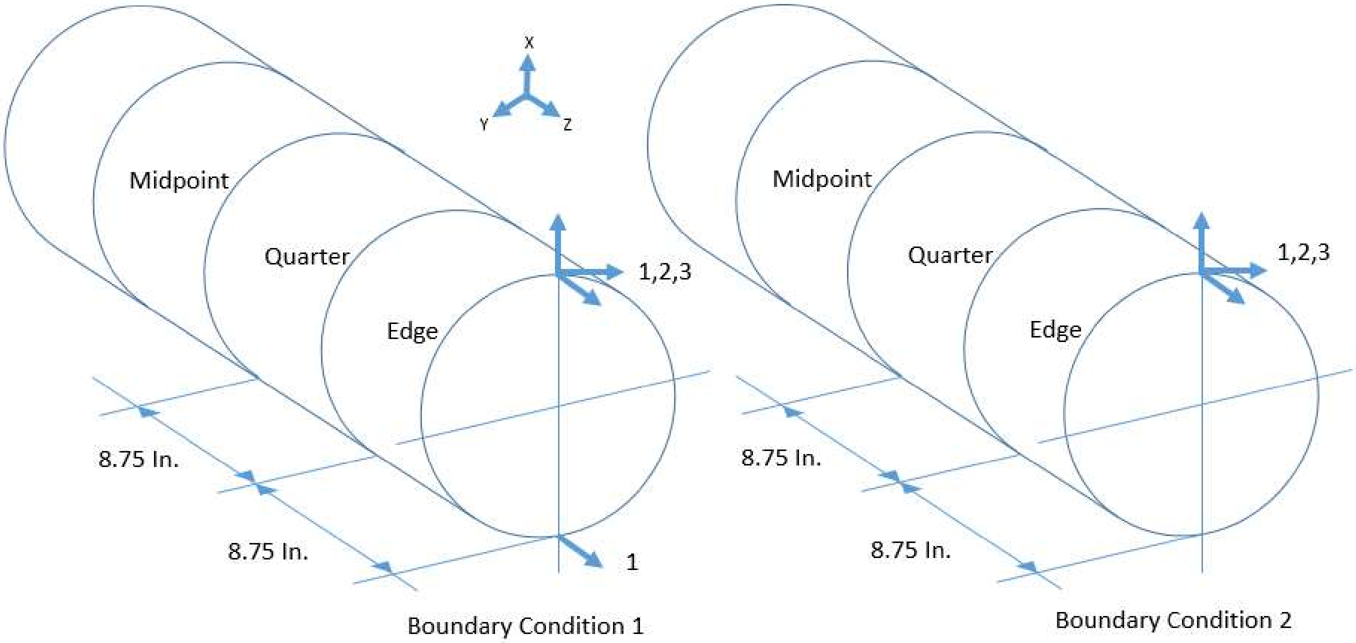

Figure 29. Boundary Conditions to prevent rigid-body motion

4.3.1 Shell A

The experimental out-of-roundness plot is shown in Figure 30. The out-of-roundness plots demonstrate a consistent pattern between experimental and numerical data, with characteristic symmetry with respect to 180º angular position (Fig. 30). The location of crown is at 0º and 180º, which is also the location of the thickest layup in the cylindrical shell, as a result of designed fiber tow overlaps. This layup configuration results in locally stiffer crown region in longitudinal direction, that is expected to produce a more thermo-elastic anisotropy during cool down and is responsible for the observed out-of-roundness deformation pattern. Overall, the predicted deformed shape shows good qualitative agreement with the experimentally observed deformation patterns (Fig. 31) using both linear and nonlinear FEA, as well as constant and temperature-dependent material properties.

Both numerical and experimental deformed shapes exhibit outward deformation with respect to best fit cylinder at the 180º and 360º locations, with the highest radial deformation, 0.04 in., located near the edges of the shell. At the midpoint location at 90° and 270° there were inward deformation in both experimental and modeling results, with the lowest inward radial deformation measured to be -0.045 in. The radius of the FEA model was 8.180 in. prior to cooling analysis, given by the midplane radius. With a standard deviation of 0.00076 there was no significant difference between the best fit radii for different conditions for the analysis, e.g. non-linearity or temperature dependent properties (Fig. 31). The best fit cylinder for Shell A has an average radius of 8.135 in. after cooling, while the best fit for the experimental data was about 8.144 in., giving the difference of 0.009 in.

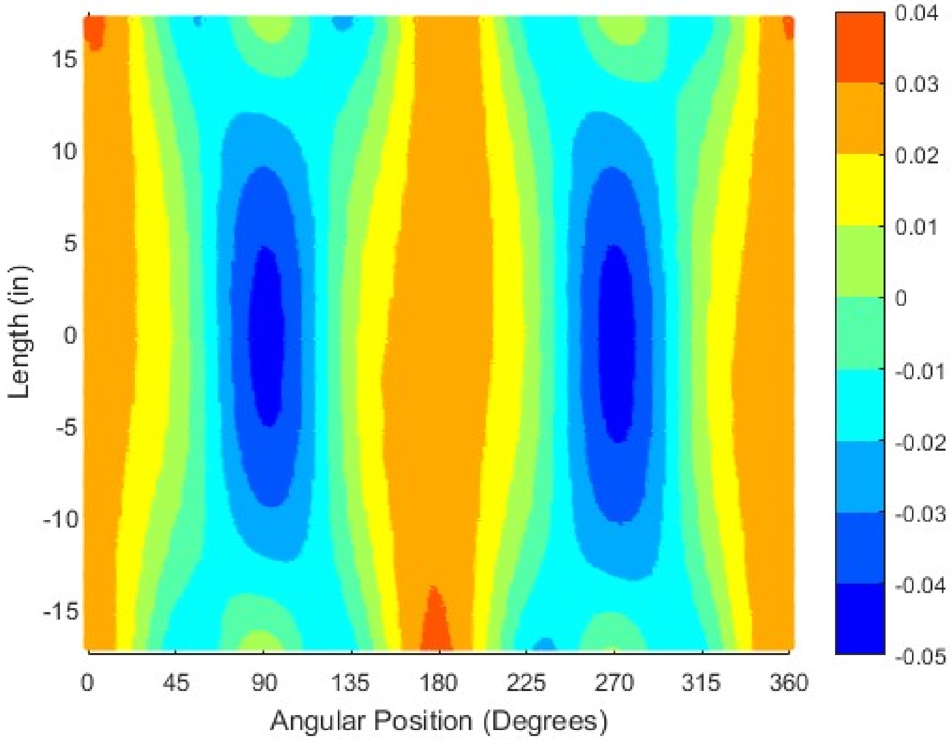

Figure 30. Experimental out-of-roundness plot for shell A, shell with overlaps

Certain areas of the numerical model, such as the edge, display higher average amplitudes of the out-of-roundness than that of the manufactured prototype. However, the overall patterns of the model give adequate representation for the geometry due to residual deformation. The amplitudes of the experimental and the numerical models had a peak difference of 0.028 in. which occurred around the edge with an average value of 0.011 in. The midpoints and the quarter point comparisons display even better correlation with lower average difference of 0.009 in. for the midpoint and 0.005 in. for the quarter (Fig. 32). These results indicate good correlation of the model prediction with the experimental data, despite Shell A having a layup which produced more variation in thickness. The existing differences between the experimental and numerical model can be attributed to the complex layup and unaccounted processing factors preceding cooling, e.g. chemical shrinkage [16]. However, the overall similarity of the shape demonstrates that residual deformation in complex composite structures, such as Shell A, to be modeled using shell based FEA.

Shell A	Constant properties	Temperature dependent properties
Linear analysis	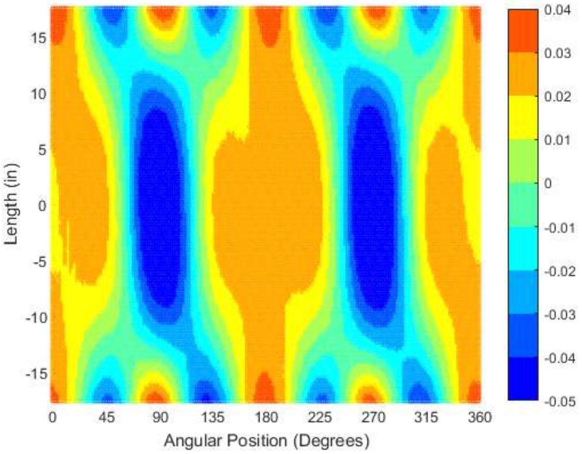	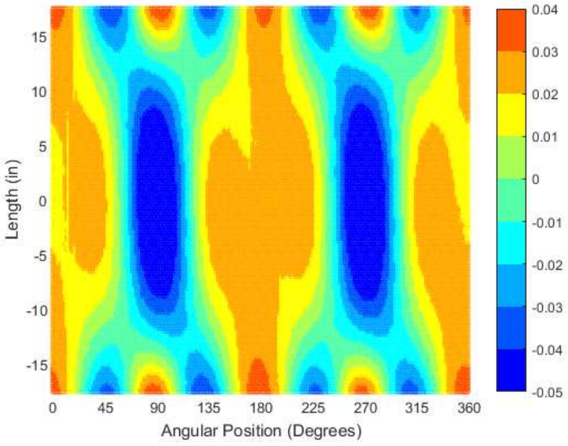
Best Fit	8.1347 in.	8.1340 in.
Non-Linear analysis	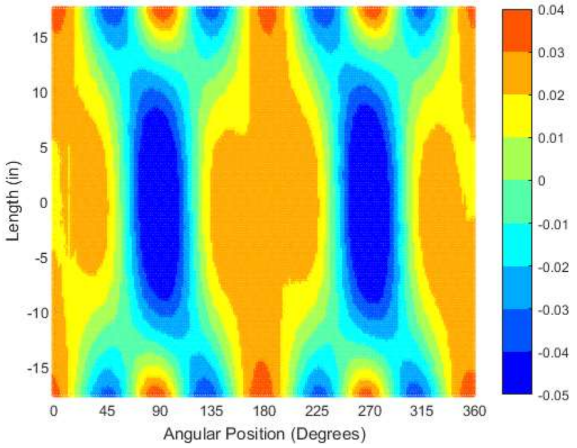	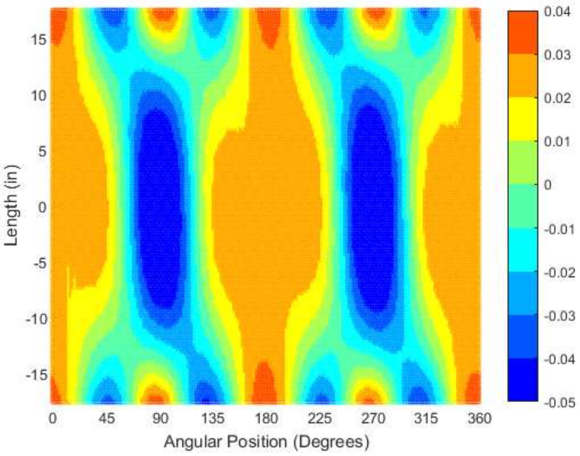
Best Fit	8.1361 in.	8.1351 in.

Figure 31. The out-of-roundness for the numerical models

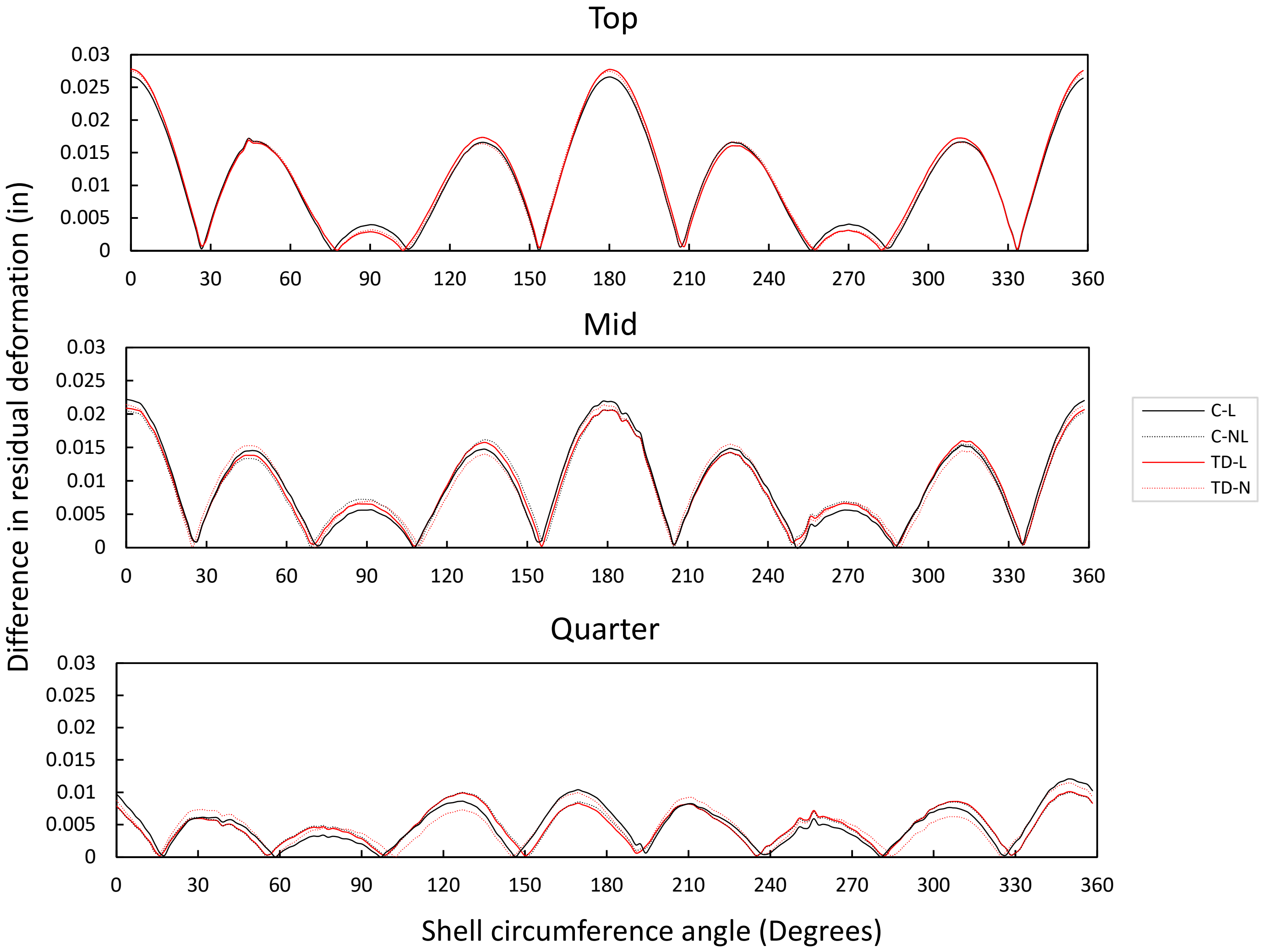

Figure 32. Difference between the Top, Mid and Quarter deformation as predicted by the analysis and experimental results for Shell A

4.3.2 Shell B

The FEA model for shell B had a similar radius of 8.180 in. The experimental out-of-roundness plot for cylindrical shell without overlaps displayed a different pattern than the one previously discussed for Shell A. The characteristic feature of the experimentally observed pattern is the antisymmetric nature with respect to 180º angular position (Fig. 33). The global deformed pattern for the shell without overlaps as predicted by the analysis did not resemble the experimental deformation out-of-roundness plots as closely (Fig. 34). Numerical analysis resulted in an antisymmetric deformation patterns, however, the experimental deformation pattern had different out-of-roundness profile. The experimental deformation pattern along the edge can be seen with a positive radial deformation between 45º to 90º, and 225º to 270º while negative, inward deformation, shown between 135º to 180º and 315º to 360º (Fig. 34). Moving away from the cylinder's edge, the out of roundness shows the periodicity in the deformation pattern with period of 180º.

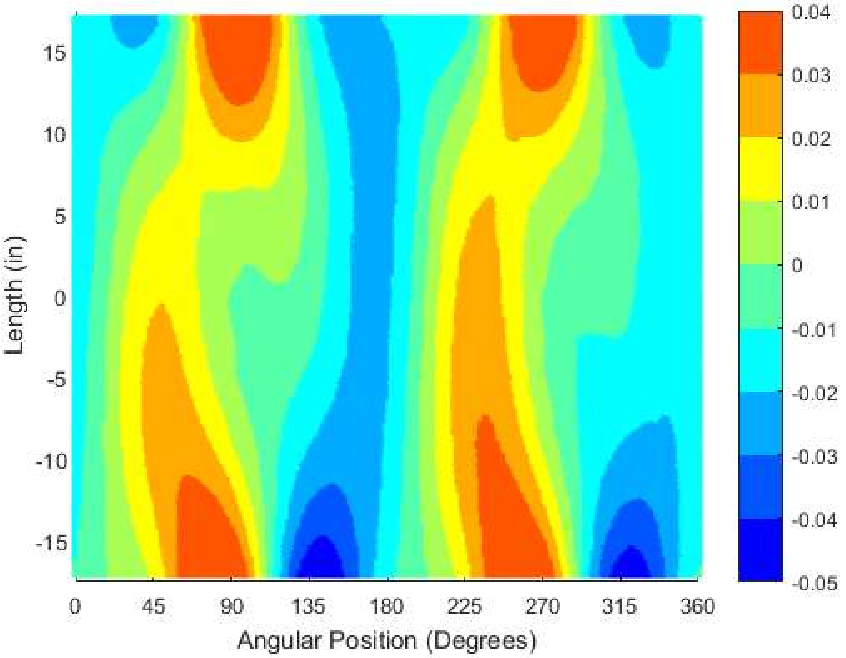

Figure 33. Out-of-roundness plot for shell without fiber tow overlaps (Shell B)

The FEA model prediction showed some similar characteristics to experimental pattern, like positive radial deformation between 45º to 90º, and 225º to 270º and negative radial deformation between 135º to 180º and 315º to 360º at the edge of the shell. However, the out-of-roundness propagation toward the middle location of the shell looked quite different between the model and experimental results. This suggests that certain factors affect residual deformation, like tool-part interaction and chemical induced shrinkages, which may play more significant role for the overall residual deformation for Shell B, as compared to Shell A. This can be due to significantly stiffer longitudinal configuration exhibited by Shell A, due to thicker crown location as a result of overlapping 10-degree tows.

The experimental out-of-roundness shows amplitudes from -0.05 to 0.04 in., while FEA models range from -0.03 to 0.03 in. Shell B modeling prediction showed similar to Shell A difference in residual deformation between experimental results near the edge, as shown in Fig. 35. The largest peak for out-of-roundness difference between experiment and the model is 0.031 in. at the edge location, with an average of 0.018 in. The midpoint location shows an average of 0.014 in. , while the quarter location displays the average of 0.013 in. (Fig. 35). The best fit cylinder for the deformed Shell B model was 8.157 in. on average, which is higher than the nomianl experimenta inner radius of 8.146 in. for manufactured prototype. The best fit difference of shell B is about -0.011 in. which his larger than the best fit difference of Shell A. The best fit difference of Shell B is also larger in comparison to the experimental best fit, indicating a lack of residual deformation in the FEA model. The difference in best fit in Shell B supports the idea that other phenomena may be responsible for the overall shrinkage. The standard deviation of shell B is 0.000206 which shows that the FEA results, the effects of linearity and temperature dependence do not seem to signficantly affect the overall pattern of the out-of-roundness, which remains consistent for all the analyses.

Shell B	Constant properties	Temperature dependent properties
Linear	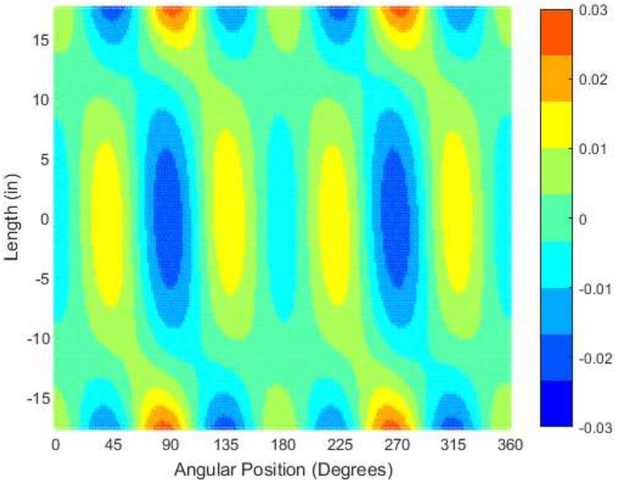	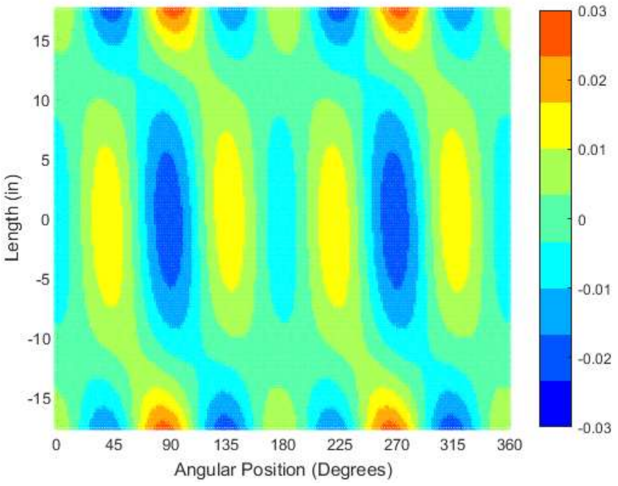
Best Fit	8.1575 in.	8.1571 in.
Non-Linear	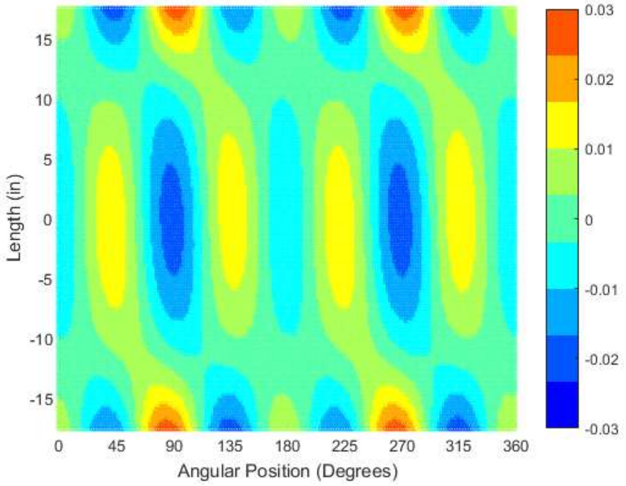	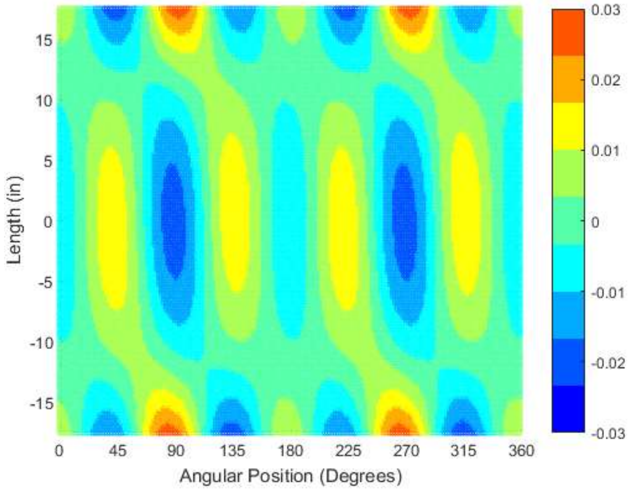
Best Fit	8.1570 in.	8.1570 in.

Figure 34. Numerical out-of-roundness plots for Shell B

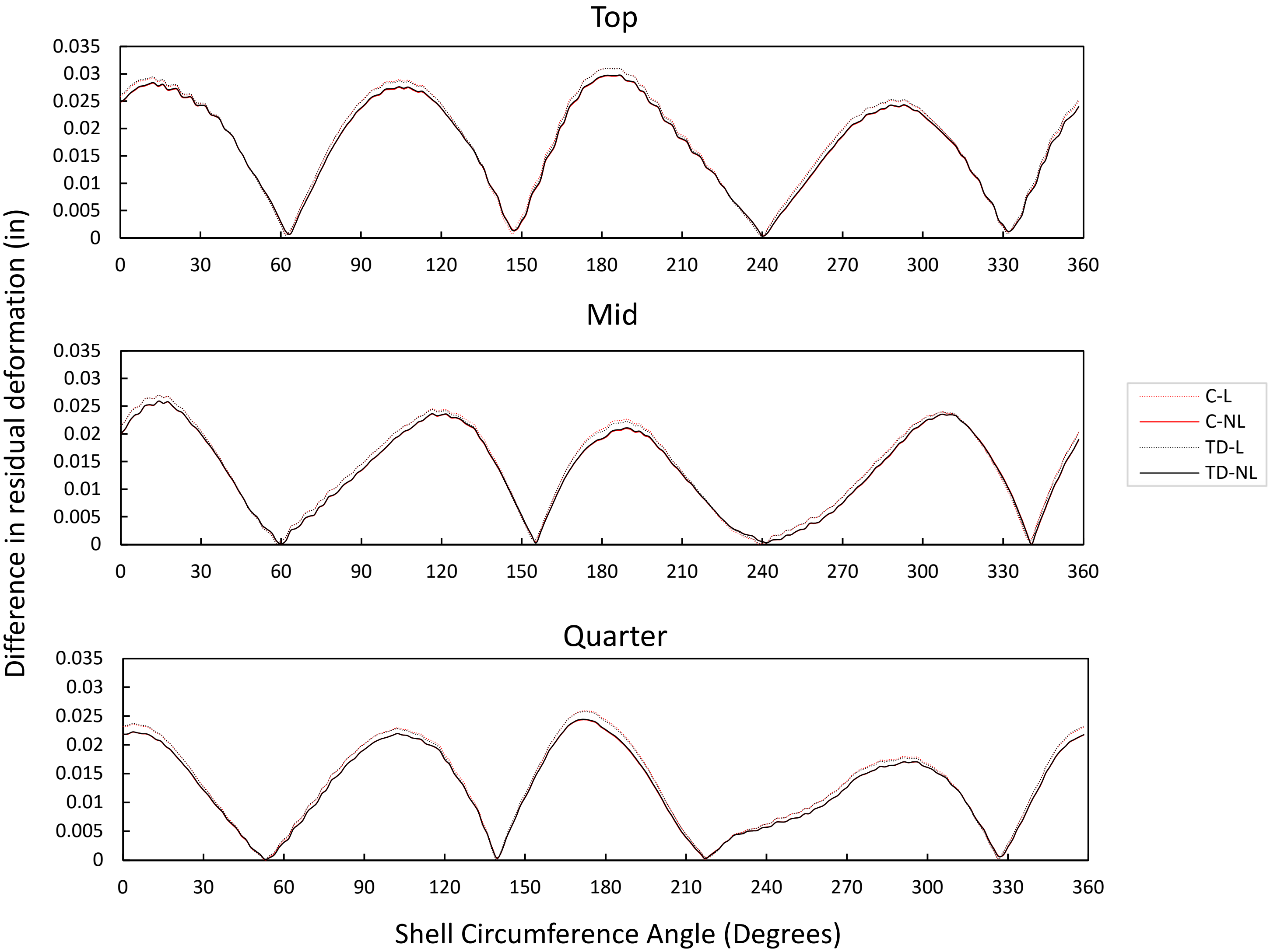

Figure 35. Difference between the Top, Mid and Quarter deformation as predicted by the analysis and experimental results for Shell B

4.3.3 Discussion of Results and Model Sensitivity to Lamina CTE

The magnitude of the out-of-roundness difference of both shells show that Shell B displays a larger value (Fig. 36). However, these differences are considerably small in comparison to the radius of the best fit cylinder (~8.144 in.). No apparent improvement in residual deformation prediction was obtained by including non-linear geometry or linear hardening of the laminate properties during cool down. This suggests that including chemical induced shrinkages can potentially provide a better correlation with experimentally observed residual deformation patterns.

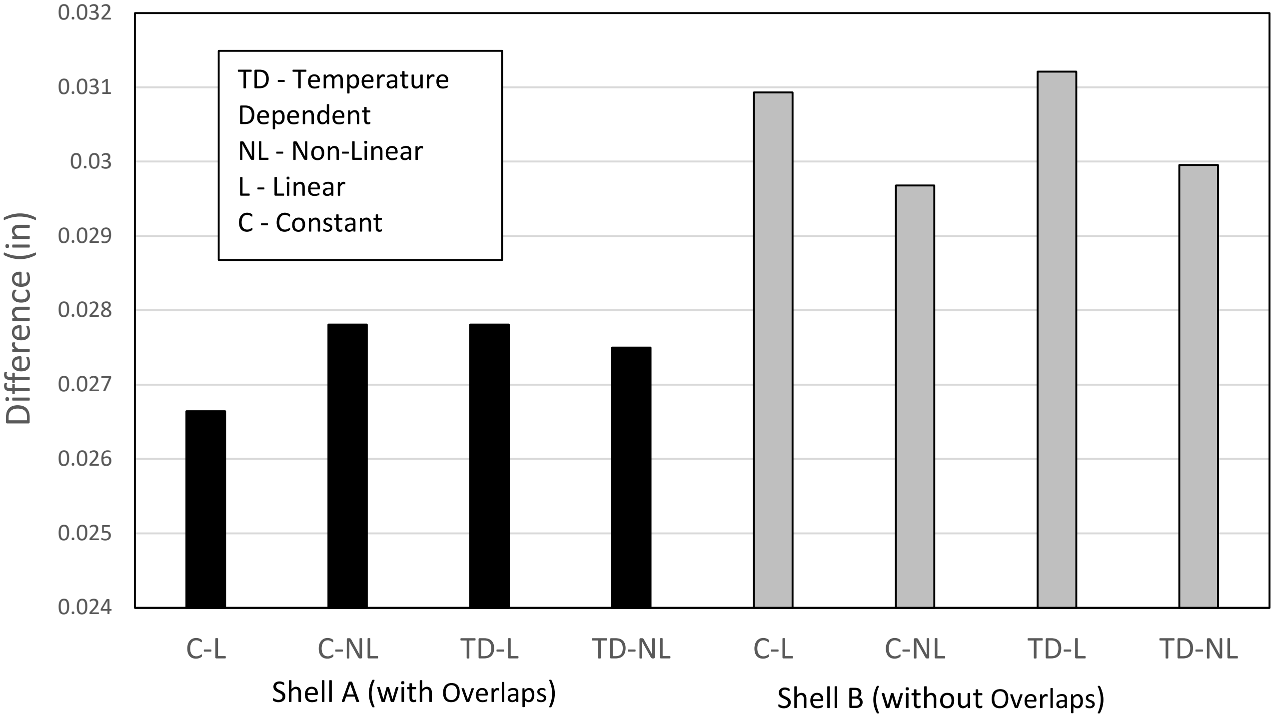

Figure 36. Peak difference values for the eight numerical models

To measure the sensitivity of the predicted residual deformation plots, the lowest and highest CTE values for $\alpha_{1,2}$ obtained from the experimental measurements were used. Both cases, with low and high lamina CTE, were ran with constant material properties and linear geometry. Furthermore, since the most difference in residual deformation is found near the edges of the shells, this location was used for sensitivity analysis. Fig. 37-38 show the difference in residual deformation for Shell A and Shell B for models with different CTE values. Results for Shell A show a trend to changing the CTE from low to high CTE values (Fig. 37). The plot shows a consistent trend with the out-of-roundness difference plot, which displays that lower CTE values decreased the difference by 12%, whereas higher values increased the difference by 8% compared to the average values. This demonstrates the Shell A model's sensitivity to changing material parameters. The plots for Shell B do not have a consistent trend between high and low CTE values (Fig. 38). Differences in the crown and keel, 0° and 180°, for Shell B show that the low CTE displays a larger difference than the higher CTE, however, the sides at 90° and 270° display less sensitivity to changing coefficients. In average, the low and high increase in the out-of-roundness was by 2% and 0.2% respectively. This indicates that the crown and keel of Shell B are more sensitive to changing CTE than its side. The results for Shell B's analysis supports the idea that residual deformation analysis using uniform values of homogenized lamina CTE cannot model the deformed configuration of steered AFP structure entirely, as well as, that other factors, like thermo-chemical induced shrinkages prior to cool down can play a role for this shell configuration. The mixed results of modeling residual deformation indicate that a significantly stiffer Shell A structure, with stiffness EI_y of 1465.803 Mlb-in^2 as compared to 780.882 Mlb-in^2 for Shell B [6], due to fiber dominated crown, can be less sensitive to local variations in the ply microstructure as a result of compaction of the fiber tow gaps and overlaps during manufacturing.

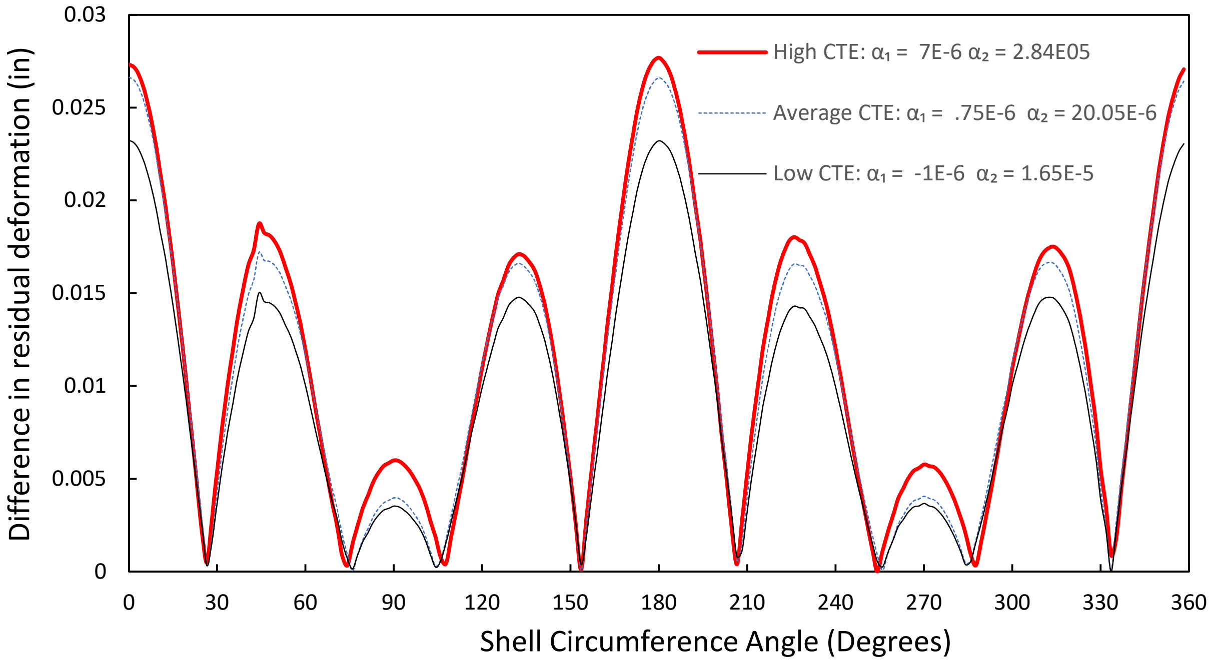

Figure 37. Shell with overlaps sensitivity plot

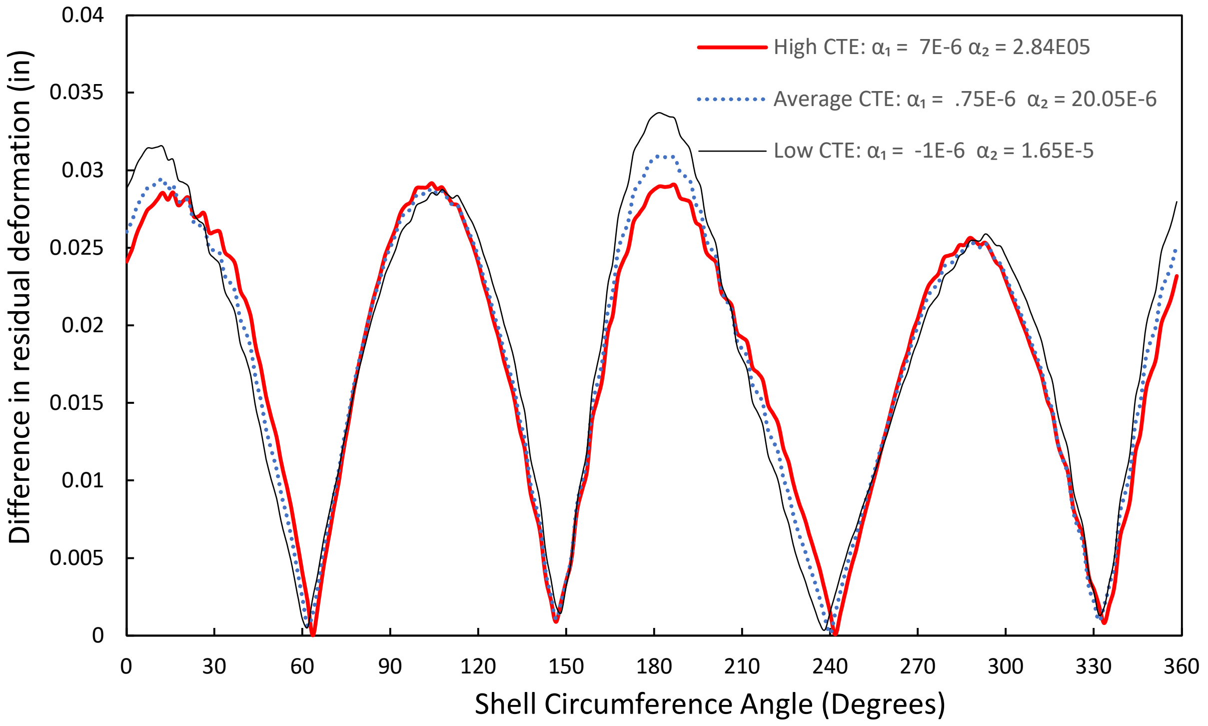

Figure 38. Shell without overlaps sensitivity plot

CHAPTER 5

CONCLUSION

The analysis of manufacturing induced defects is necessary for the certification of automated manufacturing of composites. Gaps and overlaps produce resin rich areas and voids that promote damage initiation due to localized stresses and reduces the overall strength of the material. Folds create waviness in the material which also proves to reduce the elastic properties. CT scanning and microscopy are effective methods to identify and characterize the types of layup and manufacturing defects in composites. Since the formation of defects is inevitable in composites manufactured through AFP, more research is needed to minimize defect formation through optimization of manufacturing parameters. The proposed approach for exploring defect formation in composite is through interconnected physics model for this approach is through FEA. The model consists of a thermo-chemical model and a visco-hyperelastic model. Using process modeling, the full curing cycle can be simulated with a defect induced composite.

For the prediction of the manufacturing induced defect every part of the process needs to be modeled. A thermo-chemical model is necessary to simulate the heat transfer throughout the model to capture phenomena such as the exothermic heat reaction. This causes the center of the composite to experience higher temperature than the applied and is especially true for thicker composites. In conjunction with the heat transfer, the cure kinetics was also derived in the same model using a modified Arrhenius model. Since the plots of the degree of cure and temperature display appropriate trends, the prototype of the thermo-chemical model is verified. Temperature dependent properties were used to calculate the changing properties where it is shown mostly to follow the trend of the development of the resin elastic modulus. Using invariants of the Cauchy-deformation tensor, a hyperplastic constitutive model is made. The overall behavior of the composite shows that it forms a similar geometry in comparison to CT-scan made from the same layup defect, but the middle ply does not show appropriate transverse deformation. This shows that the elastic component is inadequate for fully simulating the process model at the its current state. The missing viscous component is needed to simulate the mass flow of the resin to fully simulate the compaction of the composite. However, the heat transfer, cure kinetics, and cure dependent elastic properties were successfully incorporated within the model. The elastic properties of the composite are shown to be directly proportional to the development of the resin.

The cooling process of the manufacturing creates residual stresses that affect the resulting morphology especially in variable stiffness structures made through AFP. The validity to predict the thermally induced deformation was shown in the study. Digital image correlation was used to measure the CTE. Temperature dependence was used using previously discussed micromechanical homogenization methods. The residual deformation was measured, and a best fit cylinder was used to compare the experimentally measured data with the FEA model deformations. Two prototype shapes were analyzed, one with and without overlaps, with varying results. The shell with tow overlaps (Shell A) provided a good correlation and a close resemblance to the experimental residual deformation. However, the resultant deformation of Shell B did no show good qualitative agreement. The largest difference is exhibited at the edge with an average of 0.011 in. for shell A and 0.018 in. in for shell B. The role of linearity and temperature dependent lamina properties was analyzed, and results show the standard deviation in the difference between the modeled and experimentally deformation does not differ significantly. Specifically, the standard deformation of shell is 0.76E-3 in. for shell A and 2.06E-3 in. for shell B which suggests the insensitivity of the modeling conditions. The analysis provides a good method to determine the geometry of the resulting cylindrical composite. Overall, the present work suggests that a shell modeling approach be used to simulate process induced deformation in cooling phase in certain cases. Using non-linearity and softening material properties also exhibits that the modeling conditions does not affect the residual deformation analysis significantly. Despite these observations, the process seems indicates that a complex layup can be predicted with simple shell models.

For the automation of composite manufacturing, more testing is needed to minimize the defects that occur with the process. Process modeling is a good method for determining the manufacturing parameters that effect the morphology of the composite. However, there is much more work and research needed to continue this current study of process modeling of AFP made composites. Large temperate spikes from an exothermic heat reaction due to the gelation of composite was successfully demonstrated by the thermo-chemical model. Temperature dependence was incorporated into the visco-hyperelastic and residual deformation models. Despite the hyperelastic component of the visco-hyperelastic model being incomplete, it is a good start to a fully functional model. Lastly, the research so far has shown that finite element analysis can model the residual deformation of composite shells.

CHAPTER 6

FUTURE WORK

There is much more work to be done to develop the complete the process modeling scheme, including experimental validation. A finite element model of an AFP made composite with embedded defects needs to be constructed. This model needs to include the complex layup in a variable stiffness structure. The current elastic model geometry has a coarse mesh due to convergence issues. Therefore, it will be necessary to make the mesh finer in the future especially in areas of interest such as where the defects are located. The thermal expansion of the model has not been implemented which will use Schapery's homogenization for a temperature dependent variable. The viscous component of the visco-hyperelastic model still needs to be determined and programmed as there are numerous approaches to this subject. An unused term in the heat transfer equation is yet be incorporate which simulates the resin flow through the structure. This affects the energy balance with the Darcy velocity term, a function of viscosity that is based on the degree of cure. Creeping behavior from the constant pressure of an autoclave also needs to be added into the model. Finally, the residual stress analysis needs to be conducted, similar to the work with the tow-steered shells, to cover the whole manufacturing process of a composite. There are much more components that the overall model that is missing, but with the development of the major components of the model the model can be coupled together in a future as a single process.

Many unexplored ideas can be incorporated into the analysis, such as a stochastic process involving fiber misalignment [76]. For the residual deformation in the cooling phase, thermo-chemical shrinkage prior to cooling and variation in local ply microstructure could play a role in the residual stress analysis. More compliant structures such as Shell B may be more susceptible to this process induced phenomena. A field variable representing the mass flow through the fiber volume fraction needs to be incorporated for an interesting study into stochastic modeling of the manufacturing of composite structures. This can be used to represent resin rich environments using a low volume fraction number. A phenomenon known as locking can be also be used to model a transition between the squeezing flow and the Darcy flow in the composite where the latter is marked by the loss of resin mass due to bleeding flow in the composite sides [27]. Since there are numerous physics involved in stimulating manufacturing, there is much more potential ideas to add for the model to be as realistic as possible.

BIBLIOGRAPHY

[1] D. H.-J. A. Lukaszewicz, C. Ward, and K. D. Potter, “The engineering aspects of automated prepreg layup: History, present and future,” *Compos. Part B Eng.*, vol. 43, no. 3, pp. 997–1009, Apr. 2012, doi: 10.1016/j.compositesb.2011.12.003.

[2] D. H.-J. A. Lukaszewicz, “Optimisation of high-speed automated layup of thermoset carbon-fibre preimpregnates,” Ph.D., University of Bristol, 2011.

[3] Rani Elhajjar, “High Speed Tow Placement System for Complex Surfaces with Cut / Clamp / & Restart Capabilities at 85 m/min (3350 IPM) (2006-01-3138),” in *Additive Manufacturing of Aerospace Composite Structures: Fabrication and Reliability*, SAE, 2017, pp. 1–6.

[4] K. Wu and Z. Gurdal, “Thermal testing of tow-placed, variable stiffness panels,” in *19th AIAA Applied Aerodynamics Conference*, Jun. 2001, doi: 10.2514/6.2001-1190.

[5] K. Wu *et al.*, “Design and Manufacturing of Tow-Steered Composite Shells Using Fiber Placement,” in *50th AIAA/ASME/ASCE/AHS/ASC Structures, Structural Dynamics, and Materials Conference*, 0 vols., American Institute of Aeronautics and Astronautics, 2009.

[6] K. C. Wu, “Design and analysis of tow-steered composite shells using fiber placement,” 2008.

[7] R. L. G. Anderson, “Advanced fiber placement of composite fuselage structures,” Jan. 1991, Accessed: Mar. 22, 2020. [Online]. Available: https://ntrs.nasa.gov/search.jsp?R=19930021675.

[8] M. Bannister, “Challenges for composites into the next millennium — a reinforcement perspective,” *Compos. Part Appl. Sci. Manuf.*, vol. 32, no. 7, pp. 901–910, Jul. 2001, doi: 10.1016/S1359-835X(01)00008-2.

[9] H. B. Olsen and J. J. Craig, “Automated composite tape lay-up using robotic devices,” in *[1993] Proceedings IEEE International Conference on Robotics and Automation*, May 1993, pp. 291–297 vol.3, doi: 10.1109/ROBOT.1993.292190.

[10] M. N. Grimshaw, C. G. Grant, and J. M. L. Diaz, “Advanced technology tape laying for affordable manufacturing of large composite structures,” *Int. SAMPE Symp. Exhib. Proc.*, vol. 46, pp. 2484–2494, Jan. 2001.

[11] D. Maass, “Progress in automated ply inspection of AFP layups,” *Reinf. Plast.*, vol. 59, Jun. 2015, doi: 10.1016/j.repl.2015.05.002.

[12] A. Trochez, D. Ghosh, K. C. Wu, V. C. Jamora, and O. Kravchenko, “Effects of Automated Fiber Placement Defects on High Strain Rate Compressive Response of Advanced Composites,” *Submitt. Compos. Mater.*, 2018.

[13] K. Croft, L. Lessard, D. Pasini, M. Hojjati, J. Chen, and A. Yousefpour, “Experimental study of the effect of automated fiber placement induced defects on performance of composite laminates,” *Compos. Part Appl. Sci. Manuf.*, vol. 42, no. 5, pp. 484–491, May 2011, doi: 10.1016/j.compositesa.2011.01.007.

[14] F. Heinecke and C. Willberg, “Manufacturing-Induced Imperfections in Composite Parts Manufactured via Automated Fiber Placement,” *J. Compos. Sci.*, vol. 3, Jun. 2019, doi: 10.3390/jcs3020056.

[15] E. Oromiehie, B. G. Prusty, P. Compston, and G. Rajan, “Characterization of process-induced defects in automated fiber placement manufacturing of composites using fiber Bragg grating sensors,” *Struct. Health Monit.*, vol. 17, no. 1, pp. 108–117, Feb. 2017, doi: 10.1177/1475921716685935.

[16] O. G. Kravchenko, S. G. Kravchenko, and R. B. Pipes, “Chemical and thermal shrinkage in thermosetting prepreg,” *Compos. Part Appl. Sci. Manuf.*, vol. 80, pp. 72–81, Jan. 2016, doi: 10.1016/j.compositesa.2015.10.001.

[17] J. Lange, S. Toll, J.-A. E. Månson, and A. Hult, “Residual stress build-up in thermoset films cured above their ultimate glass transition temperature,” *Polymer*, vol. 36, no. 16, pp. 3135–3141, Jan. 1995, doi: 10.1016/0032-3861(95)97876-H.

[18] R. J. Young, R. J. Day, M. Zakikhani, and I. M. Robinson, “Fibre deformation and residual thermal stresses in carbon fibre reinforced PEEK,” *Compos. Sci. Technol.*, vol. 34, no. 3, pp. 243–258, Jan. 1989, doi: 10.1016/0266-3538(89)90031-6.

[19] F. O. Sonmez, H. T. Hahn, and M. Akbulut, “Analysis of Process-Induced Residual Stresses in Tape Placement:,” *J. Thermoplast. Compos. Mater.*, Aug. 2016, doi: 10.1177/0892705702015006207.

[20] S. C. White, P. M. Weaver, and K. C. Wu, “Post-buckling analyses of variable-stiffness composite cylinders in axial compression,” *Compos. Struct.*, vol. 123, pp. 190–203, May 2015, doi: 10.1016/j.compstruct.2014.12.013.

[21] M. Nurhaniza, M. K. A. Ariffin, A. Ali, F. Mustapha, and A. W. Noraini, “Finite element analysis of composites materials for aerospace applications,” *IOP Conf. Ser. Mater. Sci. Eng.*, vol. 11, p. 012010, May 2010, doi: 10.1088/1757-899x/11/1/012010.

[22] V. Dulgheru, B. Viorel, and G. Marin, “Some research on finite element analysis of composite materials,” *Mech. Test. Diagn. ISSN 2247 – 9635*, vol. 3, pp. 79–85, Oct. 2012.

[23] K. chauncey Wu, B. k. Stewart, and R. A. Martin, “ISAAC - A Testbed for Advanced Composites Research,” Sep. 2014.

[24] G. G. Lozano, A. Tiwari, C. Turner, and S. Astwood, “A review on design for manufacture of variable stiffness composite laminates,” *Proc. Inst. Mech. Eng. Part B J. Eng. Manuf.*, vol. 230, no. 6, pp. 981–992, Sep. 2015, doi: 10.1177/0954405415600012.

[25] T. J. Chapman, J. W. Gillespie, R. B. Pipes, J.-A. E. Manson, and J. C. Seferis, “Prediction of Process-Induced Residual Stresses in Thermoplastic Composites,” *J. Compos. Mater.*, vol. 24, no. 6, pp. 616–643, Jun. 1990, doi: 10.1177/002199839002400603.

[26] W. I. Lee, A. C. Loos, and G. S. Springer, “Heat of Reaction, Degree of Cure, and Viscosity of Hercules 3501-6 Resin,” *J. Compos. Mater.*, vol. 16, no. 6, pp. 510–520, Nov. 1982, doi: 10.1177/002199838201600605.

[27] J. P.-H. Belnoue, O. J. Nixon-Pearson, D. Ivanov, and S. R. Hallett, “A novel hyper-viscoelastic model for consolidation of toughened prepregs under processing conditions,” *Mech. Mater.*, vol. 97, pp. 118–134, Jun. 2016, doi: 10.1016/j.mechmat.2016.02.019.

[28] G. Limbert and J. Middleton, “A transversely isotropic viscohyperelastic material: Application to the modeling of biological soft connective tissues,” *Int. J. Solids Struct.*, vol. 41, no. 15, pp. 4237–4260, Jul. 2004, doi: 10.1016/j.ijsolstr.2004.02.057.

[29] J. P. Boehler, “Applications of Tensor Functions in Solid Mechanics,” 1987, doi: 10.1007/978-3-7091-2810-7.

[30] J. Bonet and A. J. Burton, “A simple orthotropic, transversely isotropic hyperelastic constitutive equation for large strain computations,” *Comput. Methods Appl. Mech. Eng.*, vol. 162, no. 1, pp. 151–164, Aug. 1998, doi: 10.1016/S0045-7825(97)00339-3.

[31] M. J. A. Latif, D. Peric, and W. G. Dettmer, “Numerical Modeling of Transversely Isotropic Elastic Material at Small and Finite Strains,” *AIP Conf. Proc.*, vol. 909, no. 1, pp. 142–146, May 2007, doi: 10.1063/1.2739841.

[32] W. Ji, A. M. Waas, and Z. P. Bazant, “On the importance of work-conjugacy and objective

stress rates in finite deformation incremental finite element analysis," *J. Appl. Mech. Trans. ASME*, vol. 80, no. 4, p. 041024, Jan. 2013, doi: 10.1115/1.4007828.

[33] V. Prot and B. Skallerud, "Nonlinear solid finite element analysis of mitral valves with heterogeneous leaflet layers," *Comput. Mech.*, vol. 43, no. 3, pp. 353–368, 2009.

[34] N. Nguyen and A. M. Waas, "Nonlinear, finite deformation, finite element analysis," *Z. Für Angew. Math. Phys.*, vol. 67, no. 3, p. 35, Apr. 2016, doi: 10.1007/s00033-016-0623-5.

[35] J. Marrouze, J. Housner, and F. Abdi, "Effect of manufacturing defects and their uncertainties on strength and stability of stiffened panels," *ICCM19 Montr. Can.*, 2013.

[36] M. Gruber, M. Lamontia, and B. Waibel, "Automated fabrication processes for large composite aerospace structures: A trade study," vol. 46, Jan. 2001.

[37] B. Kim, K. Hazra, P. Weaver, and K. Potter, "Limitations of fibre placement techniques for variable angle tow composites and their process-induced defects," in *Proceedings of the 18th International Conference on Composite Materials (ICMM18), Jeju, Korea*, 2011, pp. 21–26.

[38] O. Falcó, C. S. Lopes, J. A. Mayugo, N. Gascons, and J. Renart, "Effect of tow-drop gaps on the damage resistance and tolerance of Variable-Stiffness Panels," *Compos. Struct.*, vol. 116, pp. 94–103, 2014, doi: https://doi.org/10.1016/j.compstruct.2014.05.005.

[39] O. Falcó, J. A. Mayugo, C. S. Lopes, N. Gascons, and J. Costa, "Variable-stiffness composite panels: Defect tolerance under in-plane tensile loading," *Compos. Part Appl. Sci. Manuf.*, vol. 63, pp. 21–31, Aug. 2014, doi: 10.1016/j.compositesa.2014.03.022.

[40] M. Lamontia, M. Gruber, B. Waibel, R. Cope, S. Funck, and A. Hulcher, "Contoured Tape Laying and Fiber Placement Heads for Automated Fiber Placement of Large Composite Aerospace Structures," Jan. 2002.

[41] M. Lan, D. Cartié, P. Davies, and C. Baley, "Influence of embedded gap and overlap fiber placement defects on the microstructure and shear and compression properties of carbon–epoxy laminates," *Compos. Part Appl. Sci. Manuf.*, vol. 82, pp. 198–207, 2016, doi: https://doi.org/10.1016/j.compositesa.2015.12.007.

[42] A. Sawicki and P. Minguett, "The effect of intraply overlaps and gaps upon the compression strength of composite laminates," in *39th AIAA/ASME/ASCE/AHS/ASC Structures, Structural Dynamics, and Materials Conference and Exhibit*, American Institute of Aeronautics and Astronautics.

[43] A. Beakou, M. Cano, J.-B. Le Cam, and V. Verney, "Modelling slit tape buckling during automated prepreg manufacturing: A local approach," *Compos. Struct.*, vol. 93, no. 10, pp. 2628–2635, Sep. 2011, doi: 10.1016/j.compstruct.2011.04.030.

[44] O. Falcó Salcines, "Analysis of process-induced defects on steered-fiber panels for aeronautical applications," Universitat de Girona, 2014.

[45] C. Zhao, J. Xiao, W. Huang, X. Huang, and S. Gu, "Layup quality evaluation of fiber trajectory based on prepreg tow deformability for automated fiber placement," *J. Reinf. Plast. Compos.*, vol. 35, no. 21, pp. 1576–1585, Aug. 2016, doi: 10.1177/0731684416659933.

[46] D. O. Adams and S. J. Bell, "Compression strength reductions in composite laminates due to multiple-layer waviness," *Mesostructures Mesomech. Fibre Compos.*, vol. 53, no. 2, pp. 207–212, Jan. 1995, doi: 10.1016/0266-3538(95)00020-8.

[47] I. A. Khattab, "A novel numerical approach and experimental study on the waviness defects in composite structures," *DLR Dtsch. Zent. Luft- Raumfahrt EV - Forschungsberichte*, pp. 1–242, Jan. 2013.

[48] S. Mukhopadhyay, M. I. Jones, and S. R. Hallett, "Compressive failure of laminates containing an embedded wrinkle; experimental and numerical study," *Compos. Part Appl. Sci.*

Manuf., vol. 73, pp. 132–142, Jun. 2015, doi: 10.1016/j.compositesa.2015.03.012.

[49] S. Mukhopadhyay, M. I. Jones, and S. R. Hallett, "Tensile failure of laminates containing an embedded wrinkle; numerical and experimental study," *Compos. Part Appl. Sci. Manuf.*, vol. 77, pp. 219–228, Oct. 2015, doi: 10.1016/j.compositesa.2015.07.007.

[50] C. s Lopes, "Damage and Failure of Non-Conventional Composite Laminates," 2009.

[51] S. T. IJsselmuiden, "Optimal Design of Variable Stiffness Composite Structures using Lamination Parameters," Ph.D. Thesis, Delft University of Technology, Delft, The Netherlands, 2011.

[52] N. Bakhshi and M. Hojjati, "An experimental and simulative study on the defects appeared during tow steering in automated fiber placement," *Compos. Part Appl. Sci. Manuf.*, vol. 113, pp. 122–131, Oct. 2018, doi: 10.1016/j.compositesa.2018.07.031.

[53] M. Y. Matveev, P. J. Schubel, A. C. Long, and I. A. Jones, "Understanding the buckling behaviour of steered tows in Automated Dry Fibre Placement (ADFP)," *Compos. Part Appl. Sci. Manuf.*, vol. 90, pp. 451–456, Nov. 2016, doi: 10.1016/j.compositesa.2016.08.014.

[54] V. A. F. Costa and A. C. M. Sousa, "Modeling of flow and thermo-kinetics during the cure of thick laminated composites," *Int. J. Therm. Sci.*, vol. 42, no. 1, pp. 15–22, Jan. 2003, doi: 10.1016/S1290-0729(02)00003-0.

[55] L. E. Nielsen, "Cross-Linking–Effect on Physical Properties of Polymers," *J. Macromol. Sci. Part C*, vol. 3, no. 1, pp. 69–103, Jan. 1969, doi: 10.1080/15583726908545897.

[56] O. G. Kravchenko, S. G. Kravchenko, and R. B. Pipes, "Chemical and thermal shrinkage in thermosetting prepreg," *Compos. Part Appl. Sci. Manuf.*, vol. 80, pp. 72–81, Jan. 2016, doi: 10.1016/j.compositesa.2015.10.001.

[57] R. A. Schapery, "Thermal Expansion Coefficients of Composite Materials Based on Energy Principles," *J. Compos. Mater.*, vol. 2, no. 3, pp. 380–404, Jul. 1968, doi: 10.1177/002199836800200308.

[58] J.-B. Donnet and R. C. Bansal, *Carbon fibers*. Crc Press, 1998.

[59] M. Sutton, W. Wolters, W. Peters, W. Ranson, and S. McNeill, "Determination of displacements using an improved digital correlation method," *Image Vis. Comput.*, vol. 1, no. 3, pp. 133–139, Aug. 1983, doi: 10.1016/0262-8856(83)90064-1.

[60] O. G. Kravchenko, S. G. Kravchenko, A. Casares, and R. B. Pipes, "Digital image correlation measurement of resin chemical and thermal shrinkage after gelation," *J. Mater. Sci.*, vol. 50, no. 15, pp. 5244–5252, Aug. 2015, doi: 10.1007/s10853-015-9072-3.

[61] C. Flament, M. Salvia, B. Berthel, and G. Crosland, "Digital image correlation applied to thermal expansion of composites," in *Proceedings of the 19th International Conference on Composite Materials (ICCM-19) 2013 (eds S Van Hoa and P Hubert), 28 July–2 August*, 2013, pp. 5235–5243.

[62] Z. Ran, Y. Yan, J. Li, Z. Qi, and L. Yang, "Determination of thermal expansion coefficients for unidirectional fiber-reinforced composites," *Chin. J. Aeronaut.*, vol. 27, no. 5, pp. 1180–1187, Oct. 2014, doi: 10.1016/j.cja.2014.03.010.

[63] R. R. Johnson, M. H. Kural, and G. B. Mackey, "Thermal Expansion Properties of Composite Materials.," LOCKHEED MISSILES AND SPACE CO INC SUNNYVALE CA, 1981.

[64] T. Das, S. Bandyopadhyay, and S. Blairs, "DSC and DMA studies of participate reinforced metal matrix composites," *J. Mater. Sci.*, vol. 29, no. 21, pp. 5680–5688, Nov. 1994, doi: 10.1007/BF00349964.

[65] Y. P. Varshni, "Temperature Dependence of the Elastic Constants," *Phys Rev B*, vol. 2, no.

10, pp. 3952–3958, Nov. 1970, doi: 10.1103/PhysRevB.2.3952.

[66] R. Hill, “Theory of mechanical properties of fibre-strengthened materials—III. self-consistent model,” *J. Mech. Phys. Solids*, vol. 13, no. 4, pp. 189–198, Aug. 1965, doi: 10.1016/0022-5096(65)90008-6.

[67] Z. Hashin, “Analysis of Composite Materials—A Survey,” *J. Appl. Mech.*, vol. 50, no. 3, pp. 481–505, Sep. 1983, doi: 10.1115/1.3167081.

[68] O. Kravchenko, C. Li, A. Strachan, S. Kravchenko, and B. Pipes, “Prediction of the chemical and thermal shrinkage in a thermoset polymer,” *Compos. Part Appl. Sci. Manuf.*, vol. 66, pp. 35–43, Nov. 2014, doi: 10.1016/j.compositesa.2014.07.002.

[69] R. D. Kriz and W. W. Stinchcomb, “Elastic moduli of transversely isotropic graphite fibers and their composites,” *Exp. Mech.*, vol. 19, no. 2, pp. 41–49, Feb. 1979, doi: 10.1007/BF02324524.

[70] I. Krucinska and T. Stypka, “Direct measurement of the axial poisson’s ratio of single carbon fibres,” *Compos. Sci. Technol.*, vol. 41, no. 1, pp. 1–12, Jan. 1991, doi: 10.1016/0266-3538(91)90049-U.

[71] Z. Gürdal, B. F. Tatting, and C. K. Wu, “Variable stiffness composite panels: Effects of stiffness variation on the in-plane and buckling response,” *Compos. Part Appl. Sci. Manuf.*, vol. 39, no. 5, pp. 911–922, May 2008, doi: 10.1016/j.compositesa.2007.11.015.

[72] K. G. Bang, J. W. Kwon, D. G. Lee, and J. W. Lee, “Measurement of the degree of cure of glass fiber–epoxy composites using dielectrometry,” *J. Mater. Process. Technol.*, vol. 113, no. 1, pp. 209–214, Jun. 2001, doi: 10.1016/S0924-0136(01)00657-4.

[73] S. Yi, H. H. Hilton, and M. F. Ahmad, “A finite element approach for cure simulation of thermosetting matrix composites,” *Comput. Struct.*, vol. 64, no. 1, pp. 383–388, Jul. 1997, doi: 10.1016/S0045-7949(96)00156-3.

[74] Z.-S. Guo, S. Du, and B. Zhang, “Temperature field of thick thermoset composite laminates during cure process,” *Compos. Sci. Technol.*, vol. 65, no. 3, pp. 517–523, Mar. 2005, doi: 10.1016/j.compscitech.2004.07.015.

[75] S. R. White and H. T. Hahn, “Mechanical property and residual stress development during cure of a graphite/BMI composite,” *Polym. Eng. Sci.*, vol. 30, no. 22, pp. 1465–1473, 1990, doi: 10.1002/pen.760302207.

[76] M. B. Whiteside, S. T. Pinho, and P. Robinson, “Stochastic failure modelling of unidirectional composite ply failure,” *Reliab. Eng. Syst. Saf.*, vol. 108, pp. 1–9, Dec. 2012, doi: 10.1016/j.ress.2012.05.006.

APPENDIX A: SELF-CONSISTENT FIELD EQUATIONS

Homogenized Properties using the Self-Consistent Field Equations and Property Relations

The subscripts m and f refer to the epoxy matrix and fiber properties respectively. E_{1f} and E_{2f} are the elastic modulus for the fiber in the fiber and transverse directions, respectively. G_{12f} and G_{23f} refer to the in-plane and out-of-plane shear moduli for the fiber, respectively. ν_{12f} is the major Poisson's for the fiber. E_m, G_m and ν_m are the Young's modulus, shear modulus and the Poisson's ratio for the epoxy matrix, respectively. V_m and V_f are the volume fraction for the matrix and the fiber, respectively.

Bulk Modulus

$$k_m = \frac{E_m}{2(1-\nu_m)-4\nu_m^2}$$

$$k_f = \frac{E_{1f}E_{2f}}{2(1-\nu_{23f})E_{1f}-4\nu_{12f}^2E_{2f}}$$

Elastic modulus (Longitudinal Direction)

$$E_1 = E_{1f}V_f + \frac{4(\nu_m-\nu_{12f})^2 k_m k_f G_m V_f V_m}{(k_f+G_m)k_m+(k_f-k_m)G_m V_f}$$

Elastic modulus (Transverse Direction)

$$E_2 = E_2 = \frac{1}{\left(\frac{1}{4k_2}+\frac{1}{4G_{23}}+\frac{\nu_{12}^2}{E_1}\right)}$$

In-plane shear modulus

$$G_{12} = G_{13} = G_m \left[\frac{(G_{12f}+G_m)+(G_{12f}-G_m)V_f}{(G_{12f}+G_m)-(G_{12f}-G_m)V_f}\right]$$

Out-of-plane shear modulus

$$G_{23} = G_m \left[\frac{(G_{23f}+G_m)k_m+2G_{23f}G_m+(G_{23f}-G_m)k_m V_f}{(G_{23f}+G_m)k_m+2G_{23f}G_m-(G_{23f}G_m)(k_m+2G_m)V_f}\right]$$

Plane strain bulk modulus

$$k_2 = \frac{(k_f+G_m)k_m+(k_f-k_m)G_m V_f}{(k_f+G_m)-(k_f-k_m)V_f}$$

Major Poisson's ratio

$$\nu_{12} = \nu_{13} = \nu_{12f}V_f + \nu_m V_m + \left[\frac{(\nu_m-\nu_{12f})(k_m-k_f)G_m V_f V_m}{(k_f+G_m)k_m+(k_f-k_m)G_m V_f}\right]$$

VITA

VON CLYDE JAMORA 1429 Thamesford Dr. | Virginia Beach, VA, 23464
Engineer-in-Training EMAIL: vjamo001@odu.edu | PHONE: 757-739-7214

EDUCATION

Old Dominion University

Master’s Degree in Mechanical Engineering, SEP 2018-MAY 2020

Bachelor’s Degree in Mechanical Engineering, JAN 2015 – MAY 2018

Tidewater Community College

Associate’s Degree in Mechanical Engineering, AUG 2013 – DEC 2015

Landstown High School Technology Academy, AUG 2013 – DEC 2015

RESEARCH AND WORK

Understanding the Defect Formation of Thin Ply Composites during Automated Fiber Placement SEP 2018 – PRESENT

- Developing models using process modeling to predict manufacturing defects in thin ply composites produced by automated fiber placement.
- Using Finite element program and developing models to predict thermo-structural coupled analysis and compaction behavior.
- Characterize the effects of defects on thermosetting composites using micro CT-scans

Residual Deformation Analysis in Composite Shell Structures Manufactured using Automated Fiber Placement, JUN 2018 – NOV 2019

- Develop temperature dependent models to simulate material softening
- Model residual deformation from the thermal shrinkage during the cooling process of automated fiber placement made composite

Senior Design – Compression Molding, AUG 2017 - MAY 2018

- Manufacturing of platelet-based composites through compression molding of reprocessed manufacturing trim scrap laminate
- Characterize mechanical behavior and failure modes of compression molded composites and develop finite element models to test composite structures. (Sponsored by Mar-Bal Inc.)

Biomechanical Lab Software Development Research Assistant, AUG 2017 – JAN 2018

- Supported by the National Institute of Health
- Tasked with Graphics Programming for Situs in OpenGl with C++
- Tasked with editing the python code

PUBLICATION

V.C. Jamora, K.C. Wu, O. G. Kravchenko, ‘Residual Deformation Analysis in Composite Shell Structures Manufactured using Automated Fiber Placement,” Submitted to Composite Structures (Accepted).

CONFERENCES

R. Larson, S. Way, G. D’Antonio, **V. C. Jamora**, J. D’Antonio, J. Harris, K. Allard, O. G. Kravchenko, “Mechanical Behavior of Compression Molded Hybrid Composites,” presented at *Annual Automotive Composite Conference: Proc. Of the 18th Annual Automotive Composite Conference & Exhibition, Sept 5-7, 2018, Novi, Michigan.* 2018.